IN VITRO METHOD TO QUANTIFY AND VISUALIZE VOLUMETRIC WEAR IN MENISCUS SUBJECTED TO JOINT LOADING USING A 3D OPTICAL SCANNER

by

Kate J. Benfield

A thesis

submitted in partial fulfillment

of the requirements for the degree of

Master of Science in Mechanical Engineering

Boise State University

December 2020

BOISE STATE UNIVERSITY GRADUATE COLLEGE

DEFENSE COMMITTEE AND FINAL READING APPROVALS

of the thesis submitted by

Kate J. Benfield

Thesis Title: In Vitro Method to Quantify and Visualize Volumetric Wear in Meniscus Subjected to Joint Loading Using a 3D Optical Scanner

Date of Final Oral Examination: 09 November 2020

The following individuals read and discussed the thesis submitted by student Kate J. Benfield, and they evaluated her presentation and response to questions during the final oral examination. They found that the student passed the final oral examination.

Trevor J. Lujan, Ph.D.	Chair, Supervisory Committee
Clare K. Fitzpatrick, Ph.D.	Member, Supervisory Committee
Kirk J. Lewis, M.D.	Member, Supervisory Committee

The final reading approval of the thesis was granted by Trevor J. Lujan, Ph.D., Chair of the Supervisory Committee. The thesis was approved by the Graduate College.

DEDICATION

This work is dedicated to the people who constantly encourage me day-in and day-out. To my mother and father who always answer the phone excited and in awe to hear about my research. To my sister who never really knows what I am up to but cheers me on, nonetheless. To my partner who sees me at my highs and lows and is there when I need it the most. Thank you all for pushing me to complete the work that I am proud to share.

ACKNOWLEDGMENTS

This project was supported by the National Science Foundation under grant no. 1154353. I acknowledge the dedication and selflessness of our cadaveric donor to advance science and research even after life; without our donor, this research would not be possible. I also acknowledge support from the Boise State University Machine shop for their commitment to machining the knee fixture and sample preparation devices. A special thanks is given to my committee members, Dr. Clare Fitzpatrick and Dr. Kirk Lewis, for offering their support and feedback towards the project. Additionally, I acknowledge my fellow lab mates for offering words of encouragement and advice throughout my time in the Northwest Tissue Mechanics Lab. Lastly, I would like to give my undeniable gratitude to my thesis advisor, Dr. Trevor J. Lujan, for continuously offering me praise, criticism, and support in order to make me a better researcher.

ABSTRACT

The menisci are fibrocartilaginous soft tissues that act to absorb and distribute load across the surface of the knee joint. As a result of mechanical wear and large repetitive loading, meniscus tissue can begin to breakdown, or degenerate. Meniscus degeneration increases the risk of tearing, weakened tissue integrity, and the progression of osteoarthritis. Therefore, it is imperative to understand the wear behavior of whole human meniscus to identify conditions that may significantly increase the risk of degeneration.

The objective of this study is to develop and validate an in vitro methodology for characterizing volumetric wear behavior in whole human meniscus using a 3D optical scanning system. This study was done in three parts. Part I and II consisted of assessing the accuracy and repeatability of the proposed methodology for meniscus tissue. Two surrogate models were developed for this purpose: (1) Simple Surrogate: Geometric Blocks and (2) Complex Surrogate: Menisci & Tibia Replicas. Part III utilized the method to quantify wear in whole human meniscus subjected to physiological loading conditions. One fresh-frozen cadaveric knee joint was potted in a custom designed and built knee simulator and subjected to four loading stages of 250,000 cycles. A 3D optical scanner was used to generate 3D renderings for pre- and post-wear conditions for both surrogates and human meniscus. An open-source software, CloudCompare, was then used to computationally evaluate volume loss. For the surrogate models, the process was repeated at varying wear depths, and the percentage error between real-life measured volumes and CloudCompare calculated volumes was determined. The human meniscus followed the

same scanning procedure for pre- and post-wear; however, post-wear volume was recorded following each loading stage.

Results from the simple surrogate model showed that the method was capable of measuring wear with <2% error when detecting volumetric changes of 1.08 cm^3; however, as defect depth decreased, the absolute mean percentage error increased ($p<0.001$). The complex surrogate model showed significant difference when measuring wear in the lateral and medial meniscus ($p<0.05$) with percentage errors of less than 7.9% when detecting volumetric changes of 0.4 cm^3. The results obtained from whole human meniscus testing indicate that with an increase in loading cycles, a higher degree of meniscal wear and deformation is present.

For the first time, this study provides a methodology to identify volumetric loss due to wear behavior in whole human meniscus. This is also the first study to provide comprehensive visualization and identification of global defects within the meniscus tissue. Results of this study have the potential to help identify the physical and biochemical factors that lead to meniscus degeneration thereby advancing fundamental knowledge of the etiology of degenerative wear within articulating soft tissue.

TABLE OF CONTENTS

LIST OF TABLES

LIST OF FIGURES

LIST OF ABBREVIATIONS

3D	Three Dimensional
ACL	Anterior Cruciate Ligament
A-P	Anterior – Posterior
BSU	Boise State University
CAD	Computer Aided Design
CGS	Common Geometry Subtraction
F-E	Flexion – Extension
I-E	Internal – External
LCL	Lateral Collateral Ligament
MCL	Medial Collateral Ligament
M-L	Medial – Lateral
OA	Osteoarthritis
PCL	Posterior Cruciate Ligament
V-V	Varus – Valgus

CHAPTER ONE: INTRODUCTION

1.1 Motivation

Every year the human knee joint experiences approximately 1.1 million gait cycles while encountering mechanical loading several times that of body weight [1,2]. The knee acts to provide joint stability and mobility during such large and repetitive loading. Over time, soft tissue structures of the knee, such as the menisci, can become damaged as a result of this loading. The menisci are fibrocartilaginous soft tissues that act to absorb and distribute an estimated 40% to 70% of the compressional and torsional loads across the surface of the knee joint [2–5]. As a result of mechanical wear and overuse, meniscal fibrous tissue can begin to retrogressively breakdown, or degenerate [6–10].

Meniscus degeneration is marked by the derangement of collagen fiber networks and impacts nearly 56% of the population above the age of 70 years [3,11]. Such degeneration increases the risk of multiplanar tearing, weakened tissue integrity, cartilage loss, and the progression of osteoarthritis [2,3,12,13]. Due to relatively avascular nature and minimal peripheral blood supply, menisci have limited healing capabilities to return the tissue to a pre-degenerate state [2,5]. Treatment options for advanced degraded tissue may therefore consist of the partial or total removal of meniscus tissue (meniscectomy). These procedures have the potential to increase contact stress by 65% and 235% for a partial and total meniscectomy, respectively [14]. Therefore, prevention of meniscus degeneration is critical.

In order to effectively prevent meniscus degeneration, it is imperative to quantify

the behavior of whole knee meniscus wear in order to reduce associative risks and to examine the root cause of degeneration. Such an assessment could provide a powerful tool for identifying general loading conditions, specific activities, and anatomical variations that may significantly increase wear rates and thus increase the risk of degeneration. By understanding meniscal wear behavior and the associative risks, the benefits of non-invasive (physical therapy) and invasive (meniscectomy) strategies [3,5,9,15,16] for preventing meniscus degeneration could be defined.

1.2 Research Goal

The first goal of this research is to develop and validate an in vitro methodology to quantify and visualize volumetric wear within surrogate meniscus models using a 3D optical scanner. The second goal of this research is to utilize the developed methodology for accurate characterization of volumetric wear behavior of whole human meniscus under complex joint loading conditions. The methodology developed in this study provides an innovative basis for future studies to measure wear under the impact of other potential risk factors (gender, obesity, activity, etc.) that may increase mechanical wear and injury in meniscus tissue.

CHAPTER TWO: BACKGROUND

2.1 Knee Anatomy and Joint Biomechanics

2.1.1 General Structure and Function

The knee joint is the largest and most complex bicondylar synovial joint in the human body [17]. The main function of the knee joint is to provide stability and support while acting as a multidimensional functioning hinge that flexes and extends the leg during the gait cycle. The knee is located at the junction of the two longest lever bones in the body: the tibia and the femur **(Figure 1)**. As a direct result of this positioning, the knee is subjected to constant high and repetitive loading with peak forces that can reach up to 2-4 times body weight during normal walking activity [6,18–20].

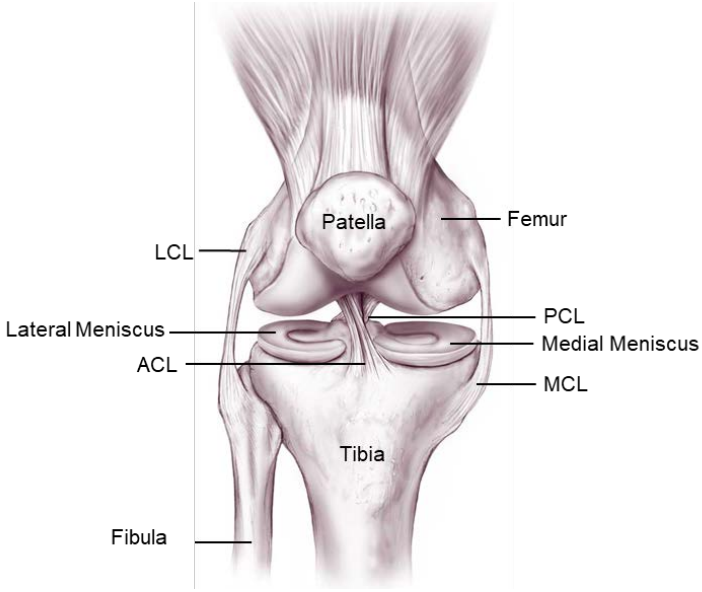

Figure 1. Anterior perspective of the human knee joint

The knee can be conceptualized as two articulations: the tibiofemoral joint and the patellofemoral joint [21,22]. The former is located between the condyles of the distal femur and proximal to the tibial surface, while the latter is formed between the patella and the anterior distal femur. The tibiofemoral joint aides in transmitting body weight forces from the femur to the tibia while allowing for primary flexion and extension motion in the sagittal plane [23]. The patellofemoral joint acts in association with the quadriceps muscle group to dissipate momentum in the frontal plane [21,24].

2.1.2 Ligaments and Joint Capsule

Stability of the knee joint is supported through various anatomical structures. Such supporting structures include the anterior and posterior cruciate ligaments (ACL and PCL), medial and lateral collateral ligaments (MCL and LCL), joint capsule, and menisci (discussed in section 2.2) **(Figure 2)**.

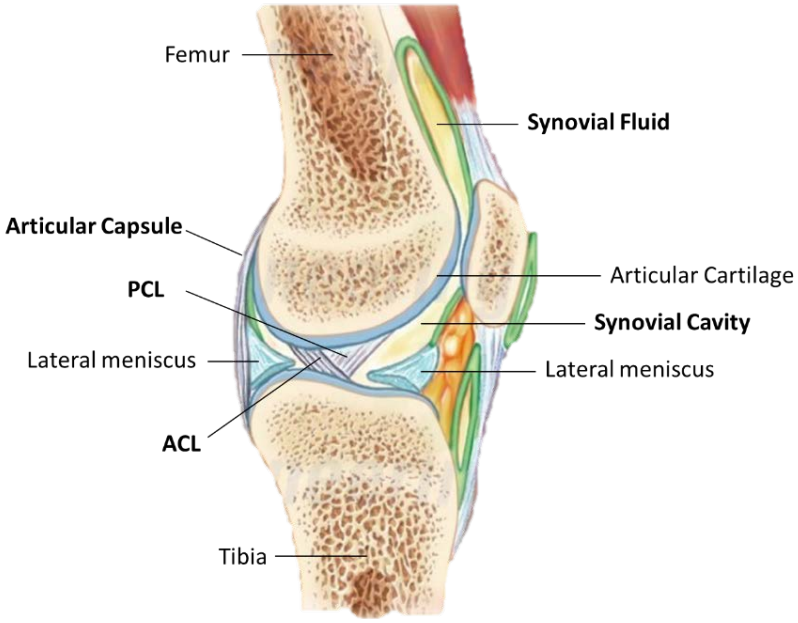

Figure 2. Sagittal view of knee joint showing supporting structures

Ligament structures of the knee provide stability due to their closely packed Type I collagen fiber bundles. These parallel orientated bundles help to compensate for tensile stresses acting in line with the axis of the collagen fibers [22,25,26]. The ACL and PCL are located within the joint capsule and cross each other obliquely to interconnect the tibia and femur [21,26] **(Figure 2)**. The cruciate ligaments act to stabilize the knee against large anterior and posterior shear forces that occur during daily activity [22]. The MCL and LCL are the primary frontal plane stabilizers that protect against forces that produce extensive varus and valgus stresses in addition to medial and lateral translation [27,28]. The joint capsule surrounds both the tibiofemoral and patellofemoral joints. It is composed of an outer layer of dense fibrous connective tissue, lined with synovium, that helps to support the knee joint by forming a sleeve around the articulating bones (tibia and femur) to which it is attached. Synovial fluid is a viscous yellow-white liquid produced by the synovium that flows throughout the capsule **(Figure 2)**. The main role of synovial fluid is to lubricate and reduce friction between the articulating surfaces of the knee joint [22].

2.1.3 Alignment of Tibiofemoral Joint

Proper alignment of the knee joint aids in balancing the forces transmitted through the soft-tissue envelope and is crucial in sustaining suitable joint function. The function of the knee joint may be analyzed through a number of axes including the vertical, mechanical, and anatomical axis **(Figure 3)**. The vertical axis is described as the vertical line extending distally from the center of the pubic symphysis and is used as a reference axis to determine other axes [29].

The mechanical axis of the lower limb, or weight bearing line, is considered to be the most accurate for defining load transmission forces across the knee joint [30]. It can be

found by drawing a line from the center of the femoral head, through the center of the knee joint at the intercondylar tubercles, and ending at the center of the ankle joint **(Figure 3)** [29,30]**.** The mechanical axis corresponds to an approximate 2 to 3 degree slope compared to that of the vertical axis [29]. The mechanical axis can be subdivided into the femoral and tibial mechanical axes. The femoral mechanical axis is defined as the line that connects the center of the femoral head to the intercondylar notch of the distal femur, while the tibial mechanical axis extends from the center of the proximal tibia to the center of the ankle **(Figure 3)** [29–31]. The hip-knee-ankle angle is thus formed between the femoral and tibial mechanical axes representing the overall alignment of the lower extremity. In normal knee alignment, this angle is usually slightly less than 180 degrees [29,30].

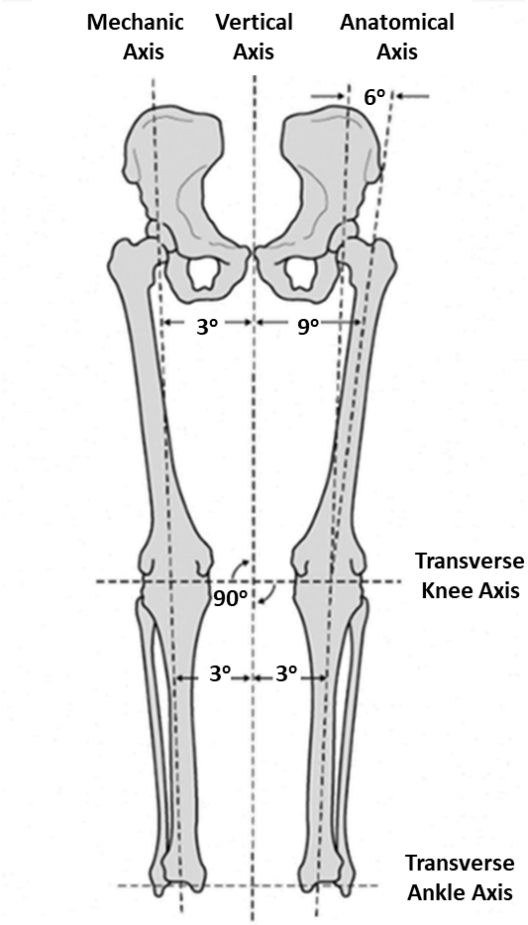

Figure 3. Anatomical and mechanical axis of the lower limb

The anatomical axis of the lower extremity represents the straight line drawn along the intramedullary canals bisecting both femur and tibia [29,31]. In the tibia, the anatomical axis is directly in line with the mechanical axis. However, in the femur, the anatomical axis has an approximate 5 to 7 degrees of inclination difference from the mechanical axis, depending on the height and pelvic width of the individual [29,31]. In normal knee alignment, the angle formed between the femur and tibia (femorotibial angle) is approximately 178 degrees in men and 174 degrees women in women [29].

2.1.4 Kinematics and Range of Motion

The tibiofemoral joint of the knee moves with a complex set of translations and rotations. The complexity of tibiofemoral joint motion can be described through six degrees

of freedom; three translations: (mediolateral (M-L), anterior and posterior (A-P), joint distraction), and three rotations: (flexion and extension (F-E), internal and external (I-E), varus and valgus (V-V)) **(Figure 4)** [32,33]**.** M-L translation and F-E rotation occur along and about the epicondylar femoral axis. Joint distraction and I-E rotation occur along and about the tibial axis. A-P translation and V-V rotation occur along and about a floating axis perpendicular to both femoral epicondylar and tibial long axes [33].

The primary motion of the tibiofemoral joint is in the sagittal plane during flexion and extension [21]. The range of motion in the sagittal plane begins at 5 degrees of hyperextension to full flexion up to 160 degrees [31,34]; examples of extension to flexion angles are given for various everyday activities as shown in **Table 1**. This flexion is due to a combination of rotation ("roll-back") and sliding of the femur over the tibia, while extension is associated with an external rotation of the tibia relative to the femur [23,31]. As the knee extends from approximately 30 to 0 degrees flexion, the tibia rotates externally by up to 30 degrees. This is known as the screw-home mechanism and is believed to occur for the purpose of tightening the soft tissue structures and locking the knee geometry prior to accommodating the impact load of weight bearing [33]. In addition to flexion and extension, the knee allows for 25 to 30 degrees of I-E rotation, 6 to 8 degrees of V-V, 5 to 10 mm of A-P translation, and 1 to 2 mm of M-L translation [31].

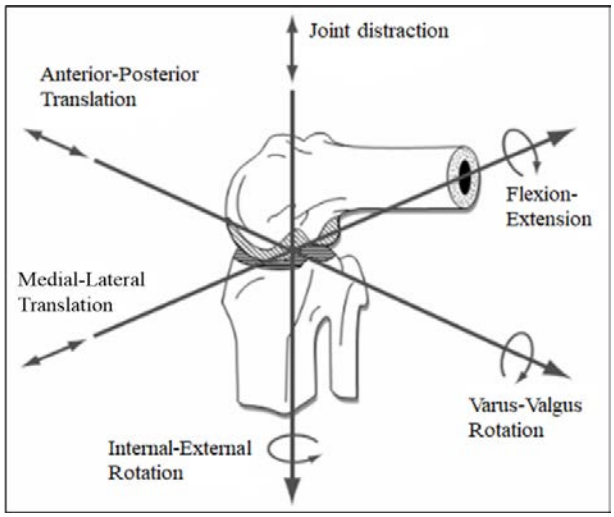

Figure 4. Six degrees of freedom in tibiofemoral joint

Table 1. Selected activities and range of motion in sagittal plane (F-E)

Activity	Range of Motion (Extension to Flexion) in Degrees
Normal Walking	0-60
Stair Climbing	0-80
Stair Descending	0-90
Sitting Down	0-115
Squatting	0-130

When the lower extremity is fully extended **(Figure 5A)** , the contact area between the femur and the tibial plateaus is large and presses anteriorly on the meniscal horns [21,33]. As the knee flexes **(Figure 5B)**, the contact between the articulating surfaces begins to move posteriorly towards the posterior meniscal horns, thus reducing the contact area of the femoral condyles with the tibial plateau. However, due to the geometric curvature of the tibial plateau, contact with the medial and lateral sides is uneven; the medial tibial plateau is slightly concave while the lateral tibial plateau is flat in the sagittal plane [33]. As a direct result, the center of contact, in terms of A-P positioning, on the medial side remains constant throughout continued flexion. On the lateral side, the femoral condyle rolls back towards the posterior horn of the lateral meniscus while the ACL is in

tension resisting further motion. As flexion increases further **(Figure 5C)**, contact between the femoral condyles and posterior meniscal horns occurs with minimal cartilage-to-cartilage contact [33].

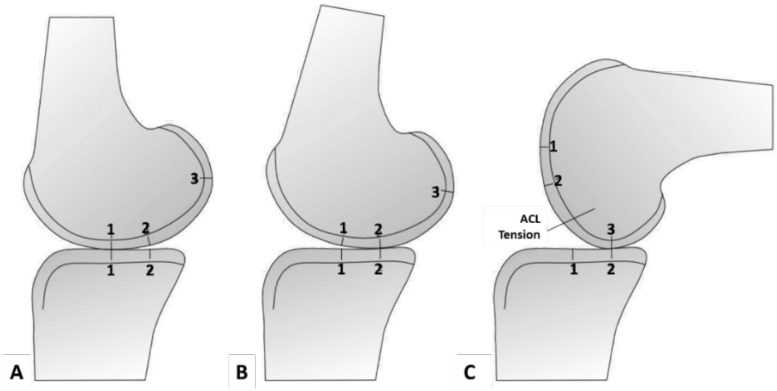

Figure 5. Tibiofemoral joint kinematics during flexion

2.2 Meniscus

2.2.1 Meniscus Structure

The knee menisci are composed of two crescent shaped fibrocartilaginous soft tissues located on the medial and lateral surfaces of the tibial plateau in both the right and left knee **(Figure 6)**. The medial and lateral menisci have distinctly different dimensions: the lateral menisci are approximately 32.4 ± 3.7 mm in length and 26.6 ± 29.3 mm wide, while medial menisci are 40.5 ± 45.5 mm long and 27 mm wide [5]. The lateral meniscus displays a greater variation in size, shape, thickness, and mobility than the medial meniscus and are thus prone to increased translation and rotation during movement [4,35]. The lateral meniscus covers a greater portion of the tibial plateau (75.9%) in comparison to the medial meniscus (51.7%) [4,5,35]. Healthy meniscus tissue is composed of 65% to 70% water with a dense extracellular matrix primarily consisting of type I collagen and traces of other sugars and proteins like proteoglycans, elastin, and sulfated glycosaminoglycan [2,4,5].

The orientation of collagen fibers is predominantly circumferential with a small amount of radial fibers located at the surface [4].

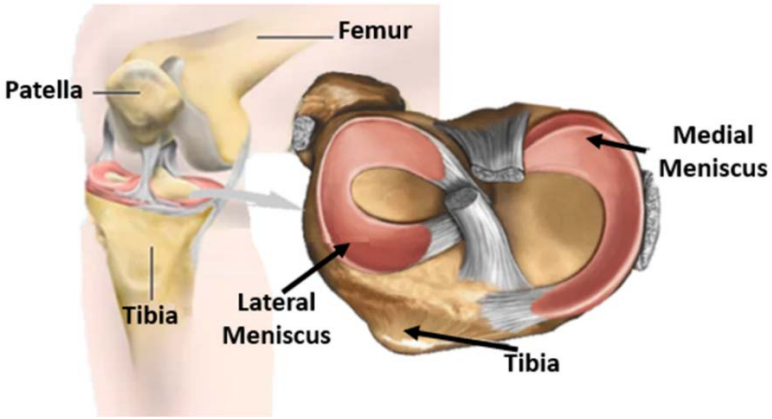

Figure 6. Diagram of lateral and medial meniscus

2.2.2 Meniscus Function

The menisci increase stability for femorotibial articulation, distribute axial, shear, and torsional loading, absorb shock, and provide lubrication and nutrition to the knee joint, while serving to decrease contact stress and increase contact area [2,5] **(Figure 7A)**. Due to the wedge-shaped geometry of the meniscus structure, it is highly capable of providing stabilization to the curved femoral condyles during articulation with the flat tibial surface. As vertical compressive loading is transmitted through the joint, the femur compresses the menisci onto the tibia and the menisci conform to the femoral condyles [2]. This results in the tissue stretching circumferentially and essentially converting the compressive forces into horizontal hoop stresses to resist further deformation **(Figure 7B)**.

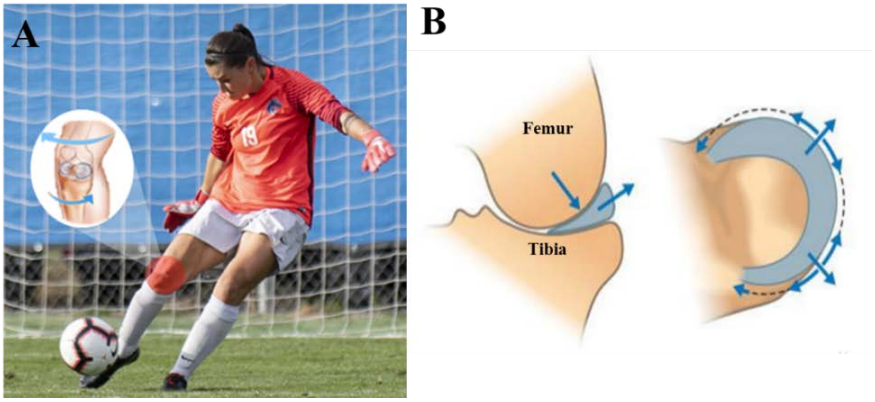

Figure 7. Function of the menisci: A) Soccer player experiencing high axial and torsional loads during kicking while B) menisci act to distribute the load

2.2.3 Meniscus Degeneration

Meniscus degeneration is a retrogressive pathological breakdown of meniscal fibrous tissue [3,13]. It begins within the substance of the tissue and is marked by the derangement of collagen fibrous networks [3,5,36]. Tissue fibrillation and disruption, in terms of fraying and tearing, is first seen at the inner peripheral rim of the meniscus followed by widespread disruption to the meniscus surface over time **(Figure 8)** [2–4,37]**.** Degeneration can lead to a host of pathological responses such as weakened tissue integrity, multiplanar tears, total disruption or loss of meniscus tissue, and ultimately the progression of osteoarthritis [37].

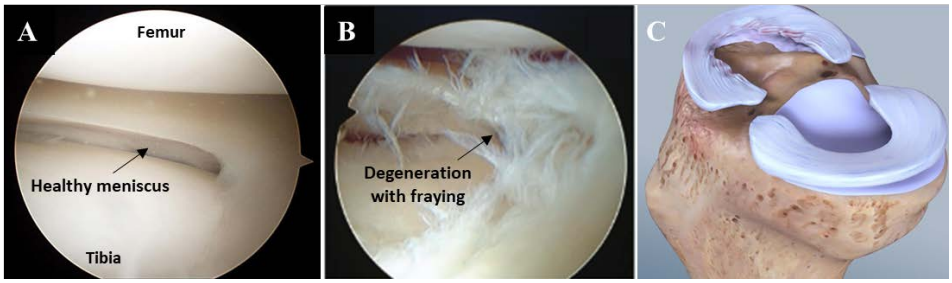

Figure 8. Arthroscopic image of A) healthy meniscus and B) degenerate meniscus with evident tearing and C) prevalence of degeneration on meniscus surface

Zhang et al. has illustrated through finite modeling that degenerative meniscal changes increase compressive and shear stresses on the articulating cartilage surfaces. This in turn causes the menisci to become more fragile and prone to tearing as greater stress concentrations on the edges of the tears occur and compromise the extracellular matrix [36]. Additionally, as the menisci further degrade, the tensile strength of the tissue decreases. This further compromises meniscus function to absorb compressive shock, thus ultimately resulting in higher contact stresses **(Figure 9)**.

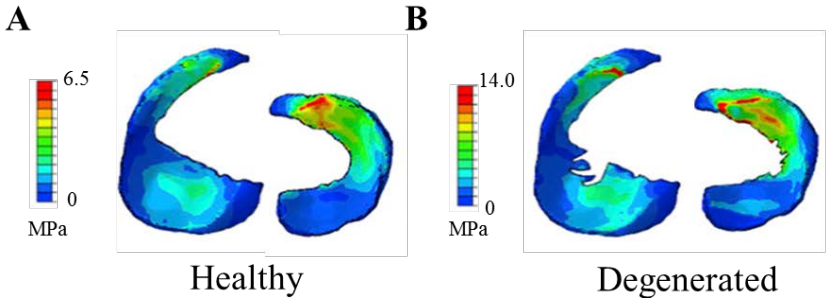

Figure 9. Contact stresses increase as A) healthy meniscus tissue B) degenerates

2.2.4 Treatment Options for Degeneration

Treatment options for meniscus degeneration are heavily influenced by the avascular nature of the tissue. The menisci can be subdivided into three distinct vascular regions: the outer, vascular/neural region termed the red-red zone, the middle, limited vascular/neural region known as the red-white zone, and the inner, avascular/anural region called the white-white zone **(Figure 10A)**. Blood vessels and lymphatics are present throughout the menisci at the time of birth **(Figure 10Bi)**; however, once the menisci become load bearing, the blood supply is reduced to the outer 25% to 33% of the menisci body **(Figure 10Bii)**; beyond the age of 50, the blood and lymph supply is further reduced to the outer 10% to 33% **(Figure 10Biii)** [38]**.** The healing capacity of the menisci is therefore extremely susceptible to injury and permanent degenerative changes. Repair

options for damage occurring outside of the avascular red-red zone are incapable of remodeling and restoring the tissue back to normal operative function [2,4,38]. Therefore, surgical intervention through either the partial or full removal of the damage meniscal tissue (meniscectomy) may be necessary. These procedures have the potential to increase contact stress by 65% and 235% for a partial and total meniscectomy, respectively [14].

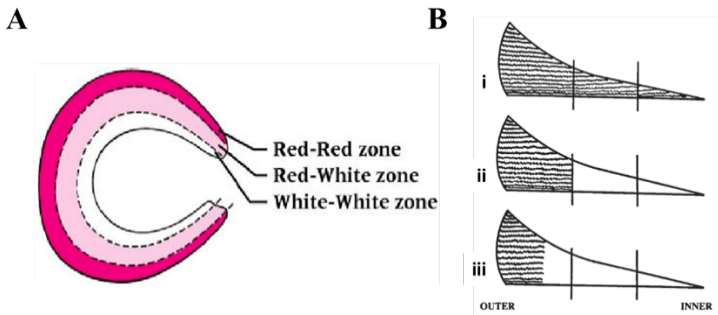

Figure 10. Meniscus blood supply in terms of A) vascularized zones and B) age related changes [38]

2.3 Mechanical Wear

2.3.1 Types of Wear

Mechanical wear is defined as the progressive removal of material from the bearing surface of one substance caused by relative motion with respect to another substance [20,39,40]. Wear can be classified by three distinct mechanisms: adhesive, abrasive, and fatigue **(Figure 11)**. Adhesive wear is characterized by two solid surfaces sliding in frictional contact while atomic bonding forces cause the material surfaces to stick to each other. As shearing is further induced by one surface, a crack propagates on the opposing surface and material is transferred from one surface to the other, thus resulting in material removal [39–42]. Abrasive wear occurs when a hard material plows, cuts, or fragments the surface of a softer material resulting in a loss of material volume in the form of debris particles [40,41]. Fatigue wear is due to an accumulation of microstructural damage to the

material as a result of cyclic contact loading [40]. Over time, superficial and subsurface cracks will appear in the material producing wear particles and loss of material volume.

Figure 11. Types of mechanical wear

2.3.2 Measuring Wear in Artificial Joint Replacements

Tribology is the study of mechanical wear on bearing surfaces. Wear is measured through a variety of different methods, and is most commonly measured by the mass of material removed per unit of time, or by the volume of the material lost [40]. Gravimetric analysis is the gold standard for wear measurement techniques. It uses a microbalance to weigh the components under study before and after a certain time period to detect the amount of mass loss that occurred **(Figure 12A)** [43]. Wear assessments of biomedical materials have traditionally been based on the gravimetric method adapted from international guideline [44]. Studies [41,45–50] have shown this method to be feasible when measuring wear in joint prosthetics; however, limitations to this method are present such as lack of information provided about shape change caused from wear [51].

Additionally, wear can be assessed through coordinate measuring machines (CMMs) that utilize a 3D digitizer and contact probe to record coordinate points on the worn surface [47,51]. Wear is then determined from the difference between the CMM digitized data and the original geometry coordinates. This method has high accuracy (5 um) yet can be extremely time consuming [47]. Other methods included in analyzing wear in joint prosthetics are micro-computerized tomography (CT) and magnetic resonance

imaging (MRI) **(Figure 12B-C)**. Micro-CT involves the use of sophisticated computer technology and x-ray equipment to combine a series of two-dimensional radiograph images into a three-dimensional model with resolutions between 50 um to 74 um [20,43,47,51]. This model can then be used to assess changes within the prosthesis as a result of wear or damage. MRI scanning is an in vivo imaging technique that uses a strong magnetic field and radio frequency to align the magnetization of hydrogen atoms within the body to generate images of soft tissue structures [51]. This technique is capable of distinguishing between high contrast between soft tissue and an implanted prosthetic device to detect implant wear.

Figure 12. Wear measuring devices for A) Gravimetric analysis, B) Micro-CT, and C) MRI scanning

2.3.3 In Vitro Wear Measurement Techniques

Classic tribological in vitro wear experiments include simple geometry pin-on-disc and pendulum studies. The pin-on-disc machine has been widely used to evaluate the nature of wear and friction on materials under well controlled, steady-state conditions [40]. The device consists of a pin attached to a static loading arm and a rotating disc. The sample is rotated and the kinetic friction coefficient is measured from the amount of deflection of the arm **(Figure 13A)** [52]. Variations of the pendulum device shown in **Figure 13B** have

been used to assess in vitro material wear. This device utilizes a pendulum arm to induce friction on a material point of contact. Wear rates for both devices are calculated from the amount of material removed during the test [40]. These tribology techniques have successfully quantified the material properties of cartilage and meniscus tissue [53–57].

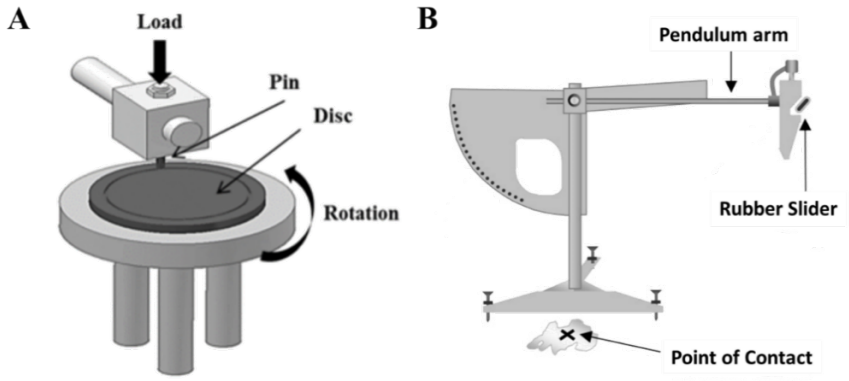

Figure 13. Established tribology methods: A) pin-on-disc and B) Pendulum

2.4 3D Optical Scanning and Modeling

2.4.1 Overview

The purpose of 3D optical scanning is to generate model renderings of an object of interest. Three-dimensional optical scanning is based on the concept of triangulation [58,59], Triangulation involves the use of cartesian coordinate systems to map spatial coordinates of an object of interest. As shown in **Figure 14**, a 3D scanning system is composed of a 3D scanner, projector, and two cameras. The angle that is formed between the cameras and either the beam of a laser (laser scanning) or projector (light scanning) is termed the triangulation angle. The triangulation angle, distance from the camera to the object and the distance from the beam source to the object are parameters used to determine the spatial coordinates of the object and to create a 3D rendering [58,60]. Currently, three-dimensional optical scanners are most commonly used for reverse engineering and product

inspection applications due to their ability to quickly and accurately generate 3D models [61–63].

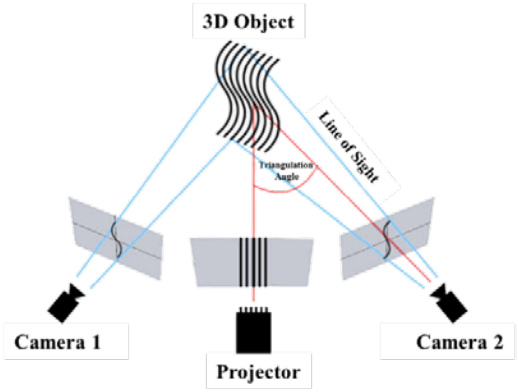

Figure 14. Diagram of 3D scanner setup

2.4.2 Structure Light 3D Optical Scanning

Structured light 3D optical scanning technology utilizes an image projector to emit a finely calibrated pattern of parallel lines with alternating stripes of light gradients onto an object of interest **(Figure 14)**. The gradual drop in gradient hue from one stripe to the next allows for the differentiation between different depth values of an object's surface features [58,61]. Cameras are used to capture the distortions of the light patterns on the object and convert the displacements of the distorted lines into surface coordinates. These coordinates are then used to quickly develop an accurate 3D reconstruction of the object of interest in the form of a point cloud [47].

2.4.3 Post-Processing and Modeling

A point cloud reconstruction consists of a set of X, Y, Z data points in space that represent the geometry of an object **(Figure 15A)** [64]. Using post-processing software applications, this point cloud can be converted into a meshed object. Meshes consist of a collection of triangular or quadrilateral polygons that are formed from connecting point

cloud data to create vertices, edges, and faces **(Figure 15B)** [64]. Meshes can be converted into solid models **(Figure 15C)** for the purpose of performing Boolean modifier operations, measuring of geometric properties, and creating computer aided design (CAD) models to assist in reverse engineering practices.

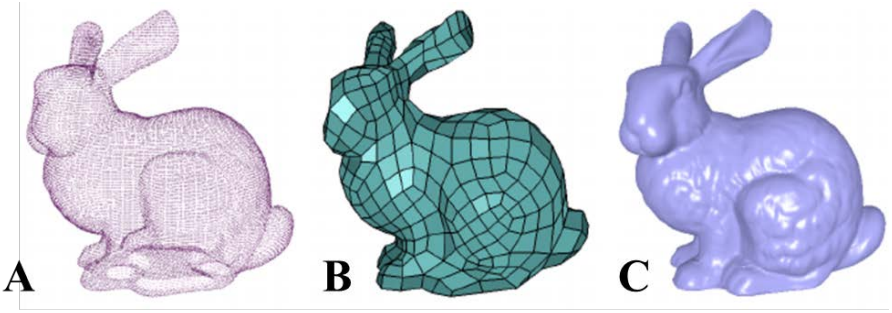

Figure 15. Modeling process for 3D scanning: A) Point cloud, B) Mesh, C) Solid Model [64]

CHAPTER 3: DEVELOPED METHOD TO QUANTIFY VOLUMETRIC WEAR

3.1 Overview

While structured light 3D scanning has been shown to be fast, accurate and low cost [12,43,47,63,65], no study has yet developed a method to use this technology to identify and measure volumetric wear in soft tissue. Therefore, the goal of this study was to utilize the 3D optical scanner to detect wear within meniscus tissue subjected to joint loading. However, in order to do this, a methodology needed to be developed and certain software programs had to be identified. A 3D scanner and accompanying scanning software, FlexScan3D, were previously identified to be capable of generating accurate 3D models of objects of interest [47]. Thus, it was understood that this technology had the potential to generate a full model of human meniscus tissue; however, it was not well understood how volumetric wear could be isolated and quantified from those 3D models.

3.2 Common Geometry Subtraction (CGS)

The developed methodology required the used of Boolean modifier operations to isolate wear. Boolean operations are performed on solid objects **(Figure 15C)** that are otherwise too complex to edit through manual operations. There are three available Boolean modifiers that create a single object from two different objects [66]**.** Union combines two objects as one seamless object while removing any overlapping geometry **(Figure 16A).** Intersection results in a mesh created only in areas where the two objects overlap and removes all sections of the objects that do not overlap **(Figure 16B)**. Subtraction removes any overlapping sections by subtracting the common geometry of one

object from that of another object **(Figure 16C)**. Using common geometry subtraction (CGS), a method was conceived to isolate wear within human meniscus.

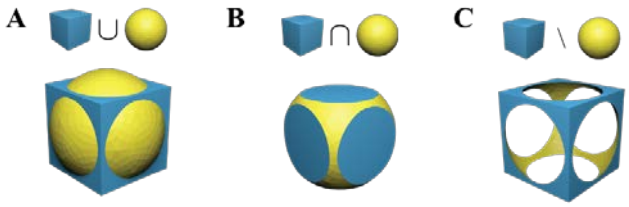

Figure 16. Boolean Modifiers showing A) union, B) intersection, C) subtraction

The method was designed based on the notion that the menisci sit on top of the tibia (section 2.2). When the tibia-meniscus and tibia-only were scanned using the 3D scanner, Boolean CGS could be used to subtract the tibia-only 3D model from the tibia-meniscus 3D model. This allowed for the complete isolation of the lateral and medial meniscus, and thus the volume of just the menisci could be quantified **(Figure 17A)**. Additionally, CGS could be used after a wearing event to quantify the volume of the post-wear isolated menisci **(Figure 17B)**. With the pre- and post-wear menisci isolated, the CGS technique could then be used to further isolate the volumetric meniscus wear between pre- and post-wear time point **(Figure 17C)**.

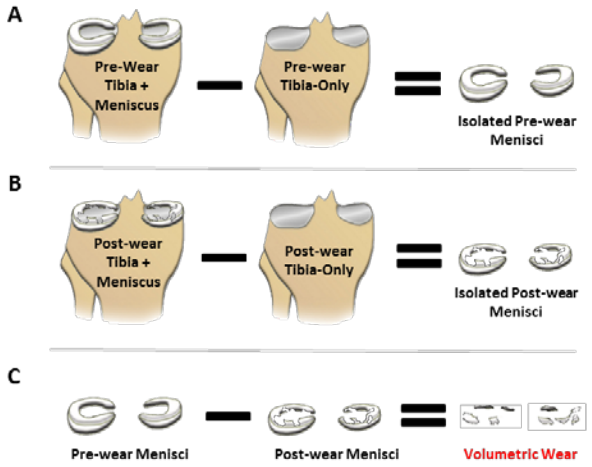

Figure 17. Basic schematic for the proposed common geometry subtraction method to isolate A) pre-wear, B) Post-wear, and C) volumetric wear

3.3 Scanning Process and Software Settings

3.3.1 Overview

The complete scanning process was done in four steps and required the use of three different software programs **(Figure 18)**. First, the object of interest was scanned using the 3D optical scanner. Next, the scanned image was processed with FlexScan3D in the form of a mesh (section 2.4.3) representing the object's surface geometry. Then, MeshLab was used to clean the mesh in terms of removing duplicate vertices, faces, and edges, and smoothing the model. Lastly, CGS was performed and the volume of the mesh was quantified in CloudCompare.

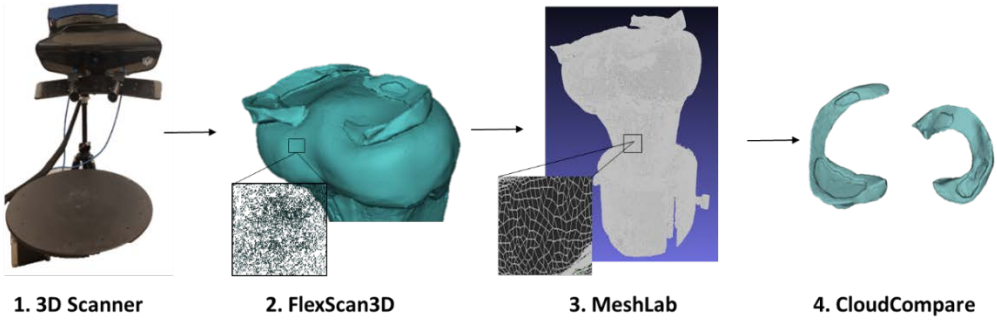

Figure 18. Four step scanning and post-processing method to quantify volume

3.3.2 FlexScan3D

FlexScan3D is a 3D scanner software package that allows for the creation of accurate digital 3D models directly from physical objects [67]. It was used to control an HDI 3D scanner and to apply post-processing techniques to form the models seen throughout the described study (section 4). In order for scanning to occur, FlexScan3D was set to *Scan* mode **(Figure 19a)**. Within the *Meshing* box, all settings were set to default expect for the mesh density **(Figure 19b)**. The mesh density was set to 20% to reduce the size of the number of vertices in the final scan in order to allow for quick post-processing. The rotatory table was activated, and the *Number of scans* was set to 8 with 45-degree rotation per scan **(Figure 19c)**. To account for high contrast between menisci and tibia bone, the *HDR* setting was selected to scan the object multiple times at varying exposure levels in order to capture the high contrast variances **(Figure 19d)**. Once the settings were implemented, the objected was scanned **(Figure 19e)** to generated multiple meshes.

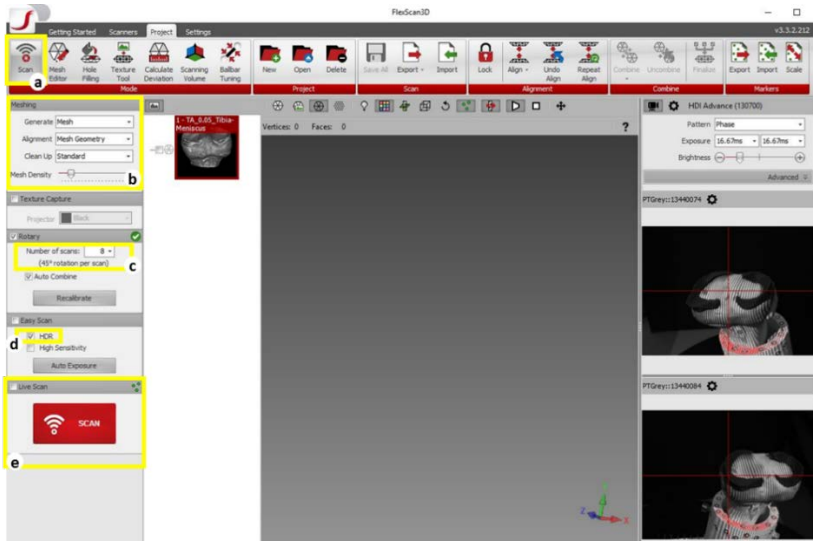

Figure 19. FlexScan3D scanning interface showing selected settings for generating a 3D scan

Following scanning, FlexScan3D post-processing techniques were automatically applied. The *Combine* feature **(Figure 20a)** was used to align and combine all scans **(Figure 20b)** into one. The fine alignment feature was used to provide a tight and accurate alignment between the scans. After all scans were combined, the *Finalize* feature was used to create the final meshed version of the 3D rendered model. The *Smoothed Merge* option was used to take in all input points and output a smoothed average of the data **(Figure 20c)**, while the *Sample Density* and *Hole Filling* sliders were set at 90% and 5%, respectively **(Figure 20d)**. A higher sample density was chosen to preserve detail within the mesh and to reduce the amount of data smoothing. When scans were combined, gaps or holes were often presented due to occlusions where the scanner could not reliability see a portion of the object. The *Hole Filling* feature fills those holes based on neighboring geometry.

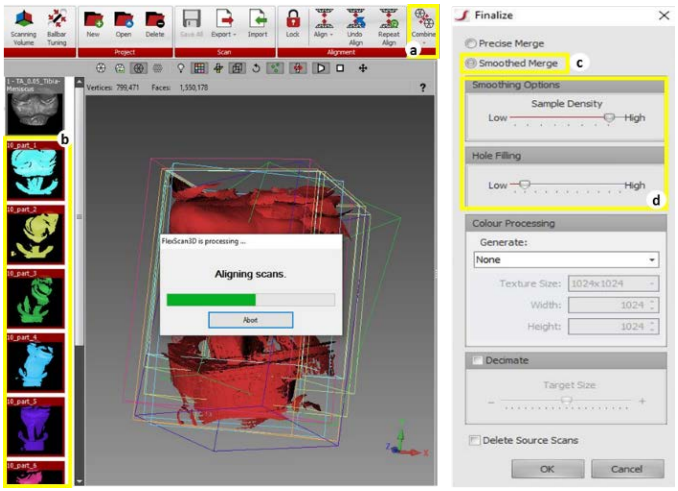

Figure 20. Aligning and combining of all individual 3D scans

With the hole fill percentage set to 5%, only small holes were automatically filled through FlexScan3D. Therefore, manual hole filling was required to produce a fully watertight mesh; this was done in the *Hole Filling* mode **(Figure 21a)**. The *Fill* slider was adjusted to set the size of the hole or gap to be relatively small in order for the *Auto Fill* feature to

automatically fill the hole. Overly complex holes were manually separated into smaller sections in order for the software to easily fill the hole using *Fill Selected* **(Figure 21b)**. These steps were done in order to generate the watertight model **(Figure 22)**.

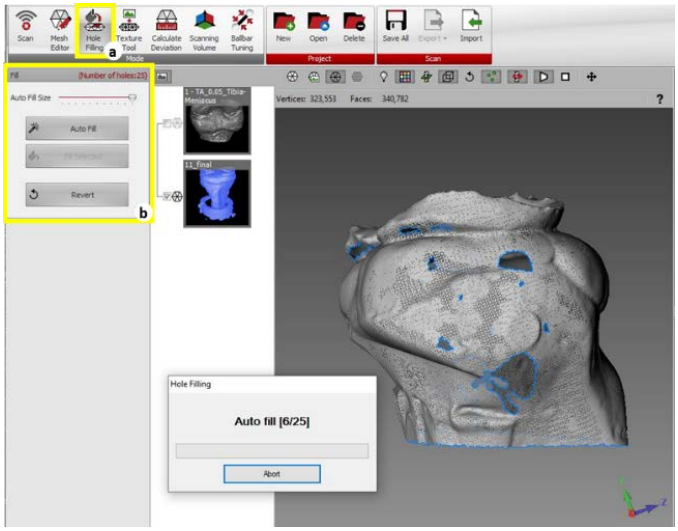

Figure 21. Hole filling feature in FlexScan3D

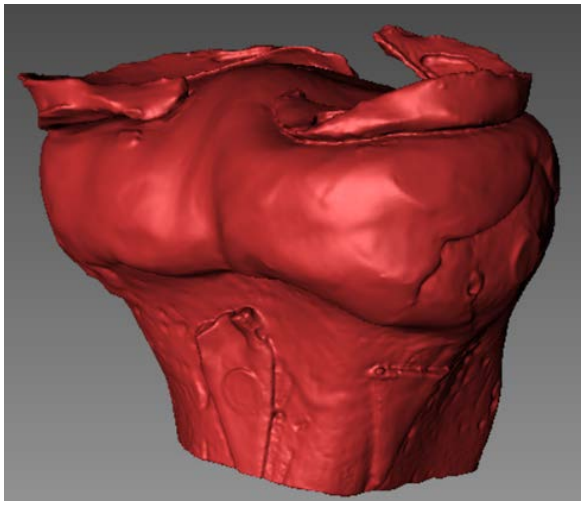

Figure 22. FlexScan3D rendered model

3.3.3 MeshLab

MeshLab is a free open-source 3D mesh processing software. It provides an immense toolbox to manage meshed objects through editing, cleaning, inspecting, rendering, and converting meshes into solid objects [68]. MeshLab was used to clean and repair the mesh obtained from 3D scanning and FlexScan3D. The mesh was cleaned by removing any duplicate vertices, faces, or edges to ensure the 3D model did not have any extra components that were not present on the real object. While FlexScan3D was capable of finalizing the mesh, additional post-processing techniques were done to further preserve object detail and repair the mesh after it was cleaned. In order to use the advanced post-processing features, normal vectors were automatically added to each vertex in the mesh through the *Compute Normals for Point Sets* feature. A *Surface Reconstruction: Screened Poisson* built-in algorithm was then applied to sharpen the mesh and ensure it was completely watertight after cleaning. All settings were found to work best on the default settings set by the software (Appendix A). A final 3D model post-processing is shown within **Figure 23**.

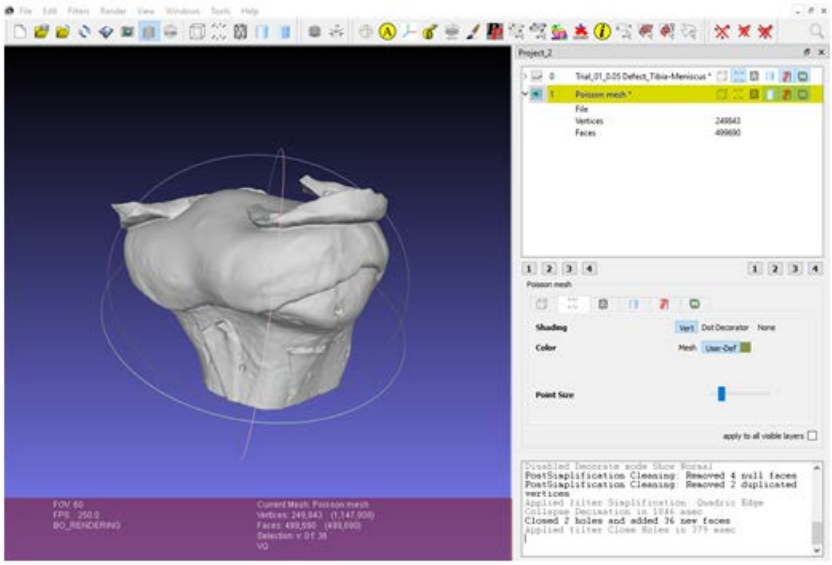

Figure 23. MeshLab interface showing completely finalized 3D model

3.3.4 CloudCompare

CloudCompare is an open-source software that is available for a wide variety of uses. It provides a basic set of tools for manually editing and rendering 3D meshes through various advanced processing algorithms [69]. The software is capable of aligning multiple processed meshes, performing common geometry subtraction (CGS), and measuring mesh volume. CloudCompare was utilized to align two meshes of an object of interest at two different times points in order to execute CGS techniques. A *Fine Registration Alignment (ICP)* was performed to align the tibia-meniscus component to the tibia-only component **(Figure 24a)**, as specified by the developed methodology in section 3.2. ICP is an iterative process in which the registration between two objects is evaluated by aligning the spatial coordinates of the objects together and applying a transformation matrix to the objected being aligned [69]. This process was done until the final RMS difference between two alignment iterations became lower than a given threshold specified by user settings (Appendix A). The *Register Info* dialogue box displays the final RMS value, transformation matrix, the applied scale used to match scales between objects, and the

theoretical overlap between the aligned and reference objects **(Figure 24b)**. This fine registration results in a tight alignment between the tibia-meniscus and the tibia-only, as shown in **Figure 24c**.

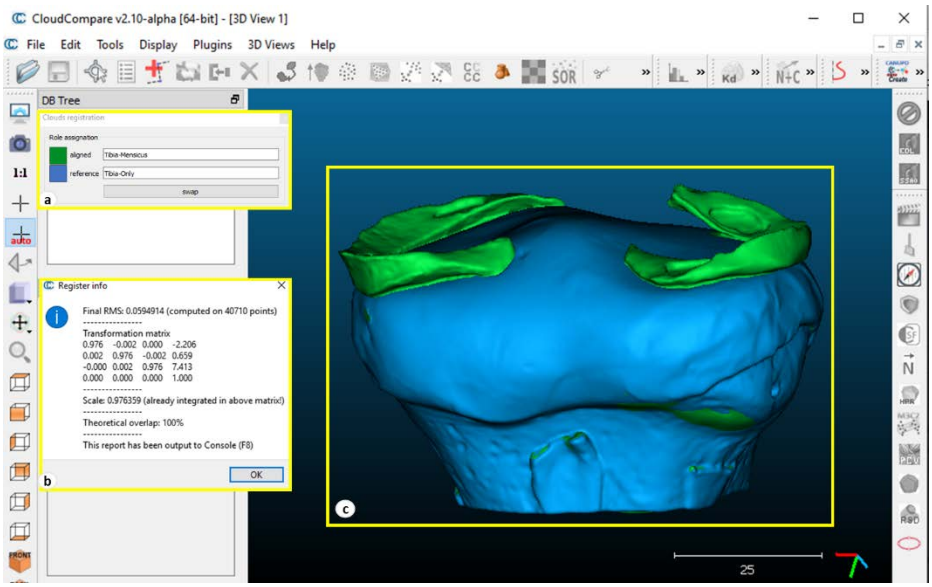

Figure 24. Fine registration Alignment (ICP) of two objects

CloudCompare algorithms employ Boolean operations through the *Mesh Boolean Operations (CGS) with Cork* feature. This feature allows for one object to be subtracted from the another based on common geometric surfaces. As shown in **Figure 25a**, the tibia-only component can be subtracted from the tibia-meniscus component using the *Difference A-B* function for the purpose of isolating the menisci **(Figure 25b)**. CloudCompare software was capable of measuring the total volume of the mesh in order to completely carry out the developed methodology to quantify volume (section 3.2).

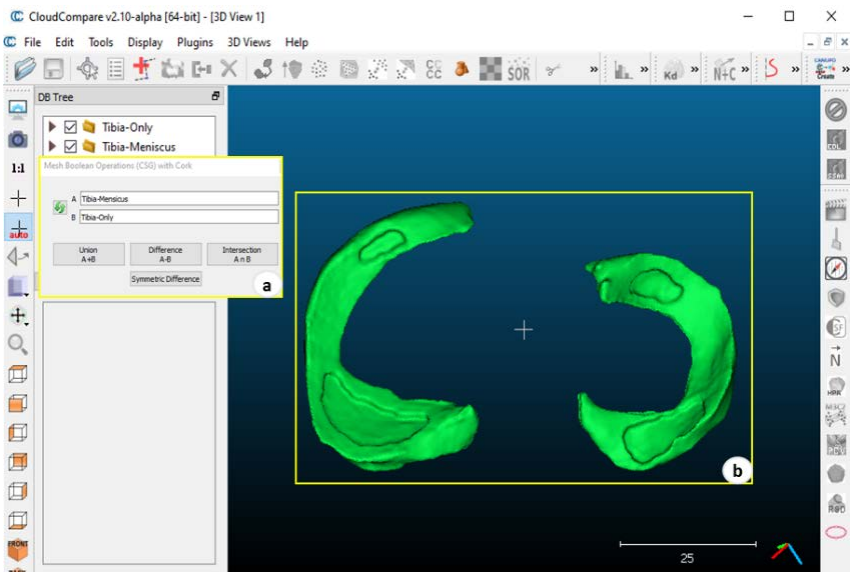

Figure 25. Common Geometry Subtraction (CGS) applied through CloudCompare software

3.4 Knee Fixture

3.4.1 Overview

Many studies [45,46,70–73] have utilized knee simulating devices to replicate physiological conditions within prosthetic and cadaveric knee joints. Such devices are capable of holding the femur and tibia components of the joint in alignment while kinematic loading is applied. To evaluate meniscus wear using the developed CGS method, mechanical loading needed to be applied to the knee joint. Therefore, a need existed to design and fabricate a custom knee fixture capable of properly aligning the tibia and femur bones while maintaining alignment throughout wear testing.

3.4.2 Custom Knee Fixture Design

A custom knee fixture was designed through solid modeling software SolidWorks and machined within the Boise State Machine shop. The fixture was used in association with an electrodynamic mechanical testing machine (Instron, Norwood, MA; E10000) to facilitate a wear testing environment that represented a specimen's nature joint alignment.

The design of the fixture needed to be able to properly position the tibia and femur in relation to each other in order to preserve tibiofemoral joint angles and to have a natural distribution of joint loading (sections 2.1.3 & 2.1.4). Additionally, due to the requirements of the developed CGS method, the menisci needed to be fully exposed for 3D scanning purposes; therefore, the tibia and femur had to be separated from each other. Since this separation disrupts the original alignment of the joint, the fixture needed to have both a tibia and femur component in order to hold each bone in place during testing and to make sure that the original joint alignment could be replicated **(Figure 26)**.

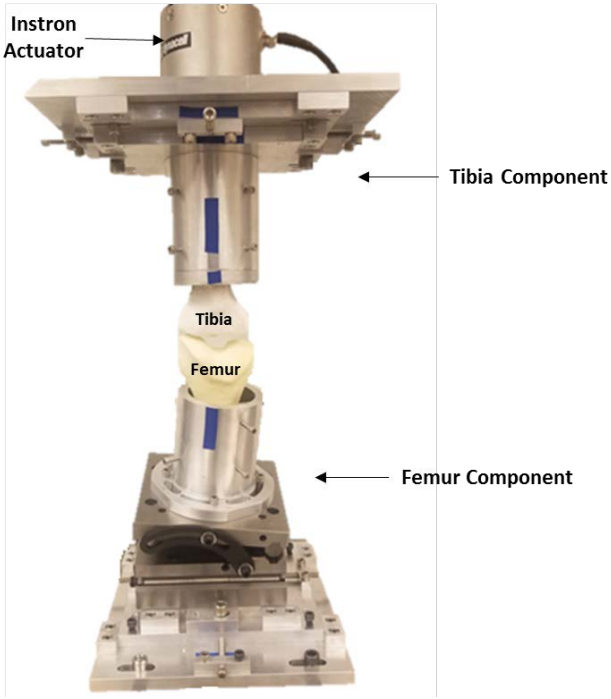

Figure 26. Custom built knee fixture consisting of a tibia and femur component allowing for 6 degrees of freedom to align and adjust kinematic bone position

The tibia component had two degrees of freedom. A custom designed XY table provided medial-lateral (M-L) and anterior-posterior (A-P) adjustment by simply adjusting a set of screws **(Figure 27A)**. Additionally, axial translation was provided by the Instron machine. The tibia pot consisted of a two-pot system with an inner and outer pot. The inner

pot allowed for the tibia to be easily removed from the fixture in order for the menisci to be scanned via the 3D optical scanner. Furthermore, the inner pot had a key that helped to center the tibia bone during potting by aligning the tibial ridge with the slot of the key **(Figure 27B)**.

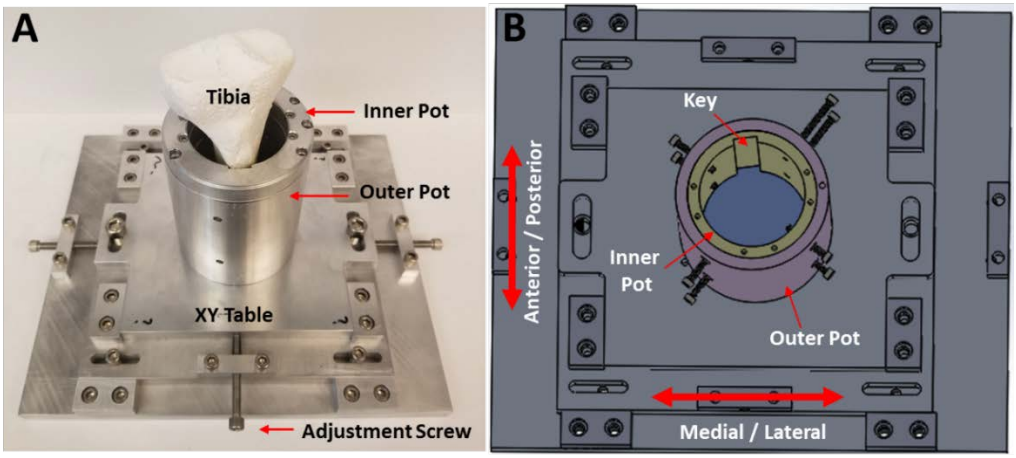

Figure 27. Tibia component showing A) SolidWorks model and B) real-life fixture

The femur component had four degrees of freedom which allowed the femur bone to be aligned to the tibia within the Instron. Like the tibia component, M-L and A-P adjustment came from the XY table while the femur pot itself provided a rotational degree of freedom. Additionally, the compound sine plate allowed for valgus-varus (V-V) adjustment in the frontal plane and flexion-extension (F-E) in the sagitial plane **(Figure 28A-B)**. A compound sine plate is most commonly used within machining; however, due to its bi-direction axes of movement, it was found to be the most practicle device to be used for the F-E and V-V movement.

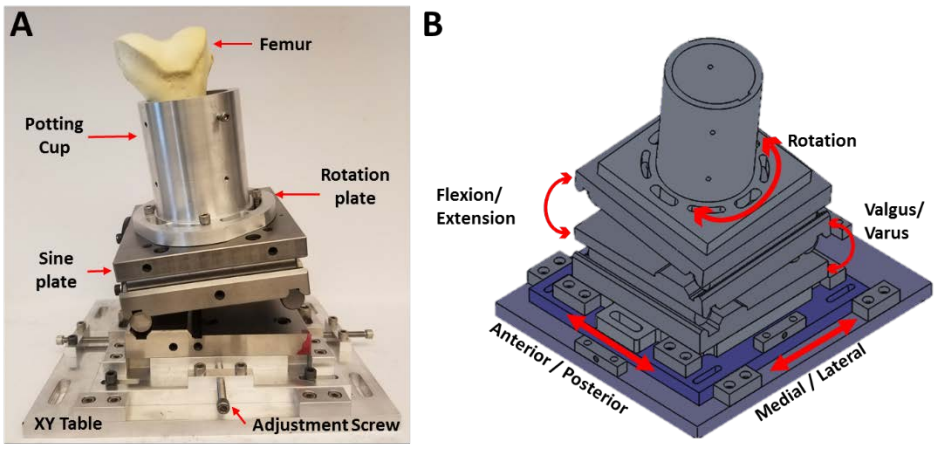

Figure 28. Femur component showing A) SolidWorks model and B) real-life fixture

An additional component needed to be added to the sine plate to adjust the V-V angle. Compressive loading and V-V motion has been found to be highly sensitive to joint positioning. It has been found that a shift in alignment of ±0.1 mm in V-V poisitioning can alter the V-V load by up to 77% [74]. To account for this sensitivity, a 3D printed thermoplastic polyurethane (TPU) insert was used to allow the positioning of the V-V angle to have play **(Figure 29)**. TPU material is durbale, flexible, and has a Shore A Durometer of 90; therfore, the insert was capable of providing less than one degree of unconstrained freedom for the V-V angle to compensate for position sensitivity changes during loading.

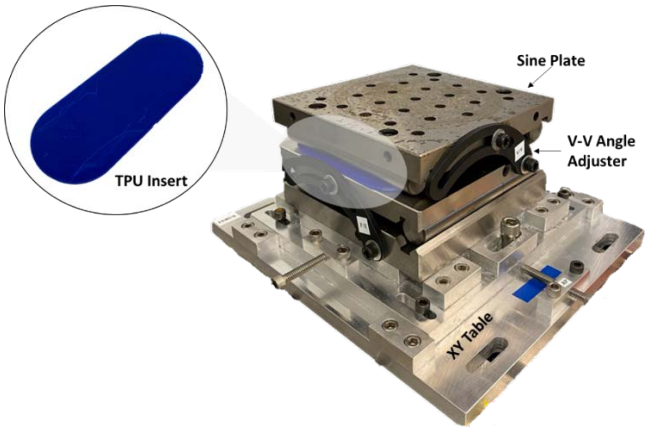

Figure 29. 3D printed TPU insert to account for V-V positioning sensitivity

3.4.3 Cutting Guide

To account for the natural angles found within the tibiofemoral joint (section 2.1.3), a custom cutting guide was designed and 3D printed using polylactic acid (PLA) filament. To prepare the joint for wear testing (discussed in section 4.2.5.1), the tibia and femur needed to be cut 17 cm below the joint line. From **Figure 30**, the call out shows a reference position for the tibiofemoral joint. The cutting guide was designed to replicate these angles by positioning the joint with the tibial anatomical axis at an approximate 90-degree angle while the femur was positioned at an approximate 84-degree angle in respect to the tibia (section 2.1.3). The cutting guide held the bones securely in place while cuts perpendicular to the tibial anatomical axis were made. The bones were then potted within the tibia and femur components of the knee fixture with the flat end of the perpendicular cut sitting flush with the base of the pots, thus maintaining kinematic joint angles and alignment.

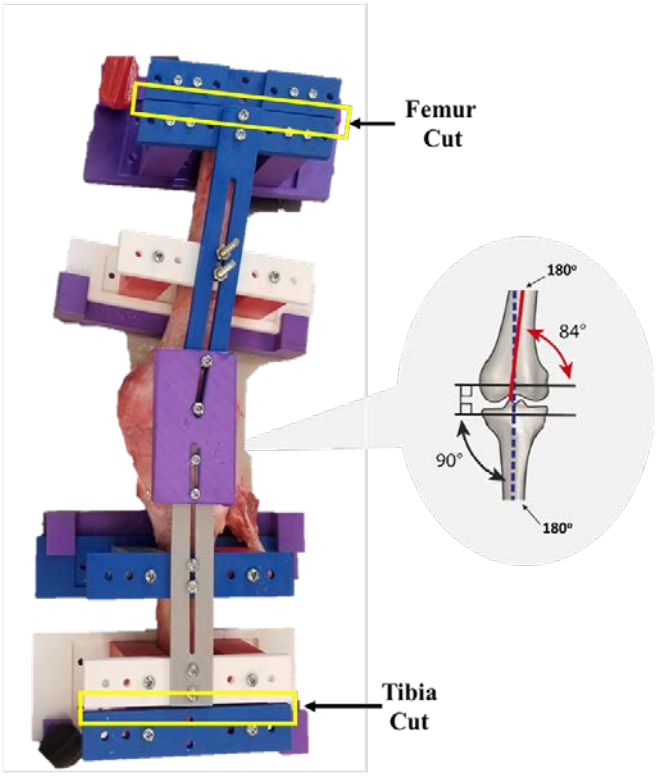

Figure 30. Custom designed cutting guide to preserve tibiofemoral joint angles

CHAPTER FOUR: MANUSCRIPT: “IN VITRO METHOD TO QUANTIFY AND VISUALIZE VOLUMETRIC WEAR IN MENISCUS SUBJECTED TO JOINT LOADING USING A 3D OPTICAL SCANNER”

4.1 Introduction

The human knee provides joint stability and mobility during approximately 1.1 million gait cycles each year [1]. Overtime, these large and repetitive loads can damage the soft tissue structures of the knee, such as the menisci. Menisci are composed of two semicircular fibrocartilaginous components that act to absorb shock due to joint compression and torsion forces while distributing load across the articular cartilage surfaces of the knee joint [2–5,13]. With an estimated 40% to 70% of joint loading exerted on the menisci, meniscal fibrous tissue can retrogressively breakdown, or degenerate, as a result of mechanical wear and overuse [2–5,7–10]. Meniscus degeneration impacts 56% of the population above the age of 70 years [11] and is marked by the derangement of collagen fiber networks leading to multiplanar tears and weakened tissue integrity [3,5,36,75]. Meniscus degeneration increases the risk of meniscus tears, cartilage loss, and progression of osteoarthritis [2,3,9,12,13]. To reduce such risks, it is important to characterize the wear behavior of whole knee meniscus and ultimately identify general loading conditions, specific activities, and anatomical variations that significantly alter meniscus wear rates. Furthermore, by understanding meniscal wear behavior and the associative risks, the benefits of non-invasive (physical therapy) and invasive (tissue removal) strategies [3,5,9,15,16] for preventing meniscus degeneration could be defined.

Mechanical wear is formally defined as the progressive removal of material from one surface of a body caused by mechanical action with respect to another surface [6,20,39,40]. Wear in conventional materials is studied through a variety of established tribology methods, such as pin-on-plate or pendulum systems applied in vitro to simple geometries, and is most commonly measured by the mass of material removed per unit time or by the volume of material lost [40,43,75]. Although these classic tribology experiments [53,54,56,57,75,76] have been used to successfully quantify the wear material properties of cartilage and meniscus tissue, they are unable to characterize the complex structural wear and deformation that occurs in whole tissue structures during joint loading.

Several experimental methods have been developed to measure wear in complex biomaterial structures subjected to joint loads [46,48,77,78]; however, they have limitations when applied to the meniscus. For joint replacement materials, the standard method to measure *in vitro* mass loss of articulating parts over millions of joint loading cycles is through gravimetrics; however, for soft tissue, unique challenges become present when measuring wear. Gravimetric analysis requires vacuum desiccation at various time points and would therefore not be suitable for hydrated soft tissue [44,46,47]. Moreover, measurement of mass loss does not allow for the identification of regional wear patterns within the tissue [43,46]. Elsner et al. showed that micro-computerized tomography (CT) can be used as a means to analyze wear in soft-tissue; however, micro-CT can be time consuming, costly, and have insufficient imaging resolution to preserve microscale detail [43,47,48,79]. A more recent study utilized an optical profilometry technique to measure localized wear in meniscus subjected to in vitro joint loading [75], but no in vitro study has measured wear and deformation in the whole meniscus.

A novel technology that has the potential to overcome the limitations of current wear analysis methods for soft tissues is structured light 3D optical scanning. Structured light scanning utilizes a projector to emit parallel lines onto an object of interest. High resolution cameras capture the distorted light pattern and the displacements of the distorted lines are converted to surface coordinates that are used to generate full 3D reconstructions of the object geometry [47]. 3D optical scanning has been proven to be fast, cost effective, and capable of detecting small surface irregularities (resolution 25 μm) [12,43,47,77,80]. While 3D optical scanning has the potential to provide an accurate alternative for measuring in vitro wear, no study has developed a method to use this imaging technology to measure wear in meniscus, or any soft tissue.

The objective of this study was to develop and validate an in vitro methodology for accurate characterization of volumetric wear behavior within whole human meniscus utilizing a 3D optical scanning system. This study will be the first to visualize and measure volumetric loss due to wear and deformation in whole human meniscus under in vitro physiological loading conditions.

4.2 Materials and Methods

4.2.1 Overview

This study consisted of three parts. The first part measured the accuracy of the wear detection method when applied to a simple surrogate model consisting of geometric blocks. The second part measured the accuracy of the wear detection method when applied to a complex surrogate model consisting of realistic meniscus and tibia replicas. The third part applied the in vitro methodology to a cadaveric human knee.

4.2.2 Scanning System

A novel procedure was developed to detect volumetric wear utilizing a 3D optical scanning system that consisted of a projector, rotary table, and two high-resolution cameras (LMI Technologies, Delta, Canada; HDI Advance R2 projector with 17.5mm lenses) **(Figure 31).** The 3D optical scanner was operated through FlexScan3D software (LMI Technologies, v3.3.2) on a computer with a 2.4 GHz processor to generate full 3D rendered models of the object of interest. Post processing software, MeshLab (ISTI-CNR, v2020.03), was used to convert the raw data from FlexScan3D into solid mesh models, and an open-source mesh processing software, CloudCompare (Telecom Paris, v2.10.3), was used to perform common geometry subtraction (CGS) between two 3D models. The experimental procedure utilized this scanning system and software tools to calculate volumetric wear **(Figure 31A-B).** This procedure required 3D models to be created at three different time points for the same specimen.

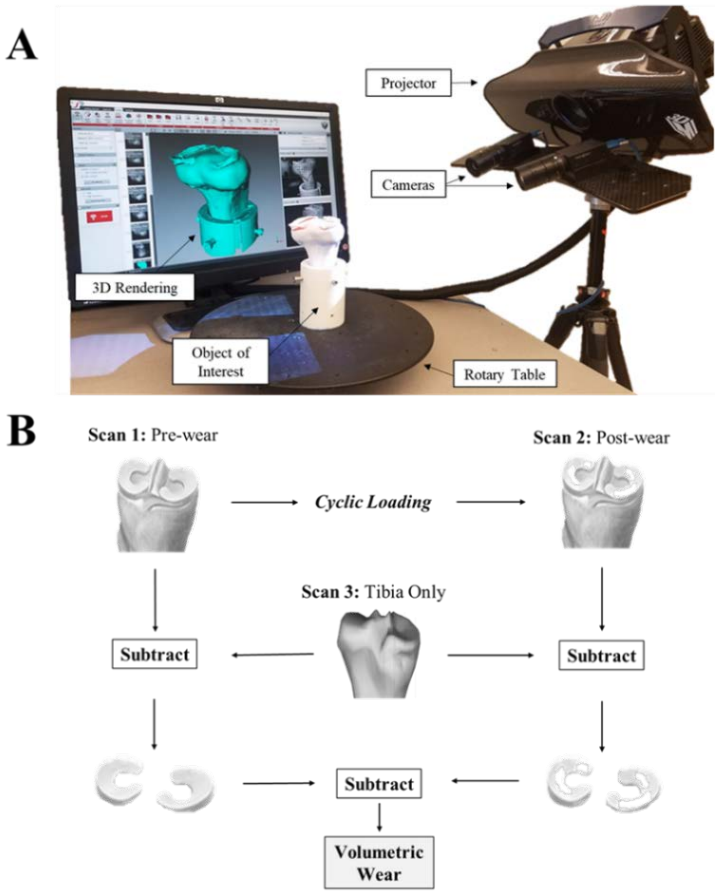

Figure 31 The 3D optical scanning system and Common Geometry Subtraction (CGS) method: A) An object is placed on the rotary table while the projector emits parallel light lines onto the object. The cameras record the distortion of these lines and the scanner software converts them into surface coordinates to generate the 3D rendering. B) Flowchart of the experimental method used to calculate volumetric wear by subtracting common geometry of the pre- and post-wear scans from the tibia only scan (i.e. Scan 1 – Scan 3, Scan 2 – Scan 3).

4.2.3 Part I & II: Accuracy of Wear Detection Using Surrogate Models

To quantify the accuracy of the 3D scanning methodology, two surrogate models were tested. A simple surrogate model determined the best-case accuracy when using basic geometric blocks, while a complex surrogate model determined how the accuracy would be affected when using a realistic meniscus-tibia model.

4.2.3.1 Simple Surrogate Model: Geometric Blocks

Delrin blocks of known dimensions were machined with six defect depths of 0.15, 0.05, 0.01, 0.005, 0.002, and 0.001 inches, corresponding to metric volumes of 1058, 356.2, 72.4, 36.2, 14.5 and 7.24 cubic millimeters, respectively. Wear depths were verified using a surface gauge with a dial indicator (Starrett, Athol, MA; resolution = ± 0.5 μm or $\pm 1.97 \times 10^{-5}$ in). Reference volume was determined from known dimensions and recorded as V_{actual}.

4.2.3.2 Complex Surrogate Model: Menisci & Tibia Replicas

A 3D CAD menisci model of a healthy male, age 29 years, BMI of 23 kg/m^2 was obtained via MR imaging from [81]. Both the medial and lateral meniscus of this model was 3D printed using polylactic acid (PLA) material (Pursa Research, Prague, Czech Republic) and positioned on a cortical foam replica of a human tibia (Sawbones, Vashon Island, WA). To reduce gap space between the 3D printed menisci and the replica tibia, a thin layer of clay was molded over the tibia to allow the menisci to sit flush against the surface of the tibia. Defects in the CAD model were made by applying a wear pattern [36] in meshing software, MaterialiseMagics (Materialise, Leuven, Belgium), and removing mesh with varying depths of 0.5, 0.025, 0.01, 0.005, and 0 inches to simulate artificially induced wear in the model menisci **(Figure 32)**. These wear depths corresponded to wear volumes of 411.7, 205.9, 79.3, 40.9, and 0 cubic millimeters, respectively. An additional 0-inch defect meniscus set was printed to serve as a control. The reference volume, V_{actual}, of the CAD defect models was measured using SolidWorks (Dassault Systèmes, v27).

Figure 32. Complex Surrogate Model showing 3D printed meniscus replicas at varying defect depths for both the lateral and medial meniscus

4.2.4 Scanning Procedure

Each surrogate followed the experimental design protocol **(Figure 33A-B)**. 3D scans were taken at three different time points: pre-wear, post-wear, and tibia-only. Pre-wear defines a model with no-defect while post-wear refers to a model with known defect depth. The 3D optical scanner was calibrated following an established protocol [47]. To reduce any surface reflectance and to enhance the quality of the scan, each object of interest was coated with a light reflectant spay (Gold Bond Foot Powder, Gold Bond, TN). Five sets of 8 scans were taken at 45-degree increments resulting in a full 360-degree view of the model consisting of 40 scans in total. This was done for a total of three trials at each defect depth for both the simple and complex surrogate.

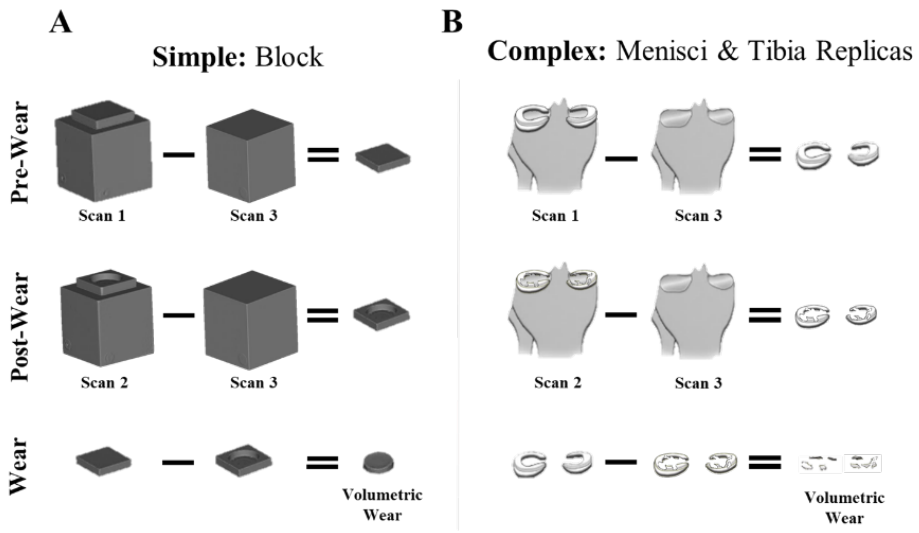

Figure 33 This method quantifies the volumetric wear for A) simple and B) complex surrogates using common geometry subtraction (CGS) between pre- and post-wear time points

All 40 scans were aligned by common geometry and combined via FlexScan3D to generate the 3D rendering of the model. If gaps were present in the full rendering, additional scans were taken and aligned with the previous scans in an attempt to fill the gap spaces. The overall time it took to complete the scanning and alignment process was approximately 40 ±5 minutes. The renderings were converted to solid meshes and cleaned during post-processing in MeshLab by removing any duplicate mesh vertices, or points. CloudCompare was utilized to align the tibia-menisci to the tibia-only in order to perform CGS. The value for measured defect, $V_{measured}$, was found by aligning the pre- and post-wear menisci and utilizing CGS to isolate the defect **(Figure 33B)**. If holes were present in either the medial or lateral meniscus mesh, they were filled using the hole filling feature in FlexScan3D. The accuracy measuring defect volume was defined as the absolute mean difference ($|V_{measured}-V_{actual}|$), while the error in measuring the defect volume was calculated ($|V_{measured}-V_{actual}|/V_{actual}$) and converted to a percentage.

4.2.5 Part III: *In-vitro* Human Application

4.2.5.1 Specimen Preparation

One human cadaveric knee (donor age=29y, female) was acquired. The knee was allowed to thaw for 24 hrs prior to dissection. All skin, fascia, muscle, tendon, and soft tissue surrounding the knee joint was removed. The joint capsule was left intact for the later purpose of recording the initial joint reference position. To maintain natural knee joint angles, the tibia and femur were transected 17 cm distal to the joint line with cuts aligned perpendicularly to the tibial anatomical axis using a custom-made cutting guide [29,30]. With the joint capsule still intact, boney landmarks where determined by palpation and marked with screws to aid in identification and alignment in scanning software.

4.2.5.2 Tibia Potting

Following marker placement, only the tibia was potted in a custom-made cylindrical mounting pot using a catalyzed polymer resin (Bondo Mar-Hyde, Atlanta, GA). The tibia shaft was centered with the tibial plateau horizonal to the base of the pot [73]. The femur was held at a 90-degree flexion angle to the tibia while Bondo was added to the pot and during the 15-minute curing time.

4.2.5.3 Reference Position

The natural reference position of the knee during full flexion was then determined by a mechanical digitizer (Revware Inc, Raleigh, NC; accuracy ±0.002-in). To do this, the potted tibia was secured within a custom-made knee fixture that allowed for six degrees of fixed adjustment to control the positioning of the tibia and femur during mounting. The fixture was attached to an electrodynamic mechanical test system (Instron, Norwood, MA; E10000) with the system's torsional-rotation axis parallel to the long axis of the tibia

following the procedure outlined in [73]. The femur was positioned directly below and aligned to the tibial axis to ensure rotational loading was represented on the proper bone **(Figure 34A)**.

With the potted tibia attached to the Instron, the femur was allowed to hang in its natural position in order for the joint to properly align itself. After the joint had ceased any movement, the femur was lightly screwed into place within its respective mounting pot so as to not disturb the natural alignment. The digitizer was then used to create embedded coordinate systems in both tibia and femur on identified bony landmarks [82]. Kinematic analysis of the tibia and femur digitizer data was done through a custom MATLAB (MathWorks, R2018b) code using established kinematic conventions of Grood-Suntay to assess the initial rotational and translational positions of the joint while the capsule was still attached [32,82].

4.2.5.4 Tibia and Femur Positioning

The joint capsule was dissected, leaving only menisci and meniscal attachments, while the tibia and femur were disarticulated. The femur was then potted (similar to the tibia, section 4.2.5.2) in its respective mounting pot with the epicondylar axis horizontal to and centered in the pot [73]. The potted femur and tibia were then fitted within the knee fixture and screwed into place **(Figure 34A)**. Kinematic analysis of the marked boney landmarks was then done to verify proper joint potting alignment. If the potted position differed from the reference position, the bones were further adjusted and redigitized until rotations and translations were within 0.5-degrees and 0.1-inches of the reference position, respectively. This step was critical in order to replicate natural knee joint kinematics and to ensure that loading was to be applied with femur and tibia in anatomical alignment.

4.2.5.5 Pre-Wear Scanning

Prior to scanning, the tibia-meniscus and femur were allowed to soak in a lubrication tank with 0.9% saline solution for 4-hours prior to scanning. This was done to mitigate artifacts from tissue swelling between time points. After the pre-soak, the potted femur remained within the lubrication tank while the potted tibia was scanned via the 3D optical scanner. Scanning followed the same procedure used for the surrogate models, excluding the coating of light reflectant spray. The meniscus tissue was sprayed with 0.9% saline solution to ensure hydration throughout the scanning process.

4.2.5.6 Mechanical Testing

The Instron was used to apply axial loading and torsional rotation based on parameters specified by ISO Standards [83,84]. It should be noted that the axial load was force controlled while the torsional rotation was displacement controlled [75]. Loading parameters for this experiment where chosen in the attempt to induce the greatest amount of wear in the tissue. It was hypothesized that this would occur at 45% of the gait cycle where the combination of axial and torsional rotation is the highest (**Figure 34B**; Flexion = 10-degrees, Axial Force = 2.4 kN, and Tibial Rotation = 1.10 degrees). Combined cyclic loading was run at a frequency set to 2 Hz for 250,000 continuous cycles resulting in a total loading time of approximately 35 hours. Four loading stages of 250,000 cycles were run for a total of 1 million cycles **(Figure 34C)**.

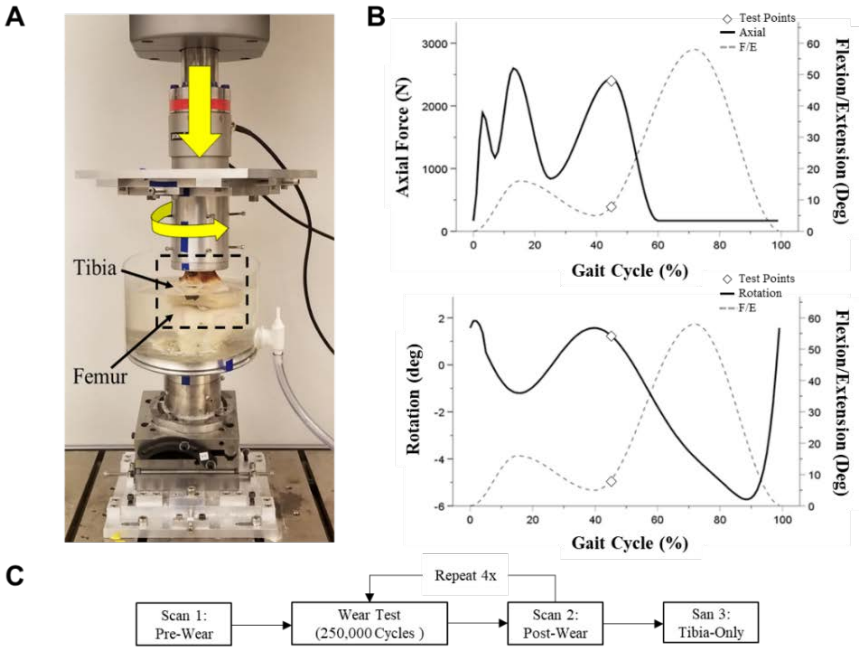

Figure 34 Mechanical testing setup and loading profile: A) Knee fixture with potted tibia and femur. B) Axial and rotational profiles based on ISO 14243-3 with test parameters identified with markers. C) Experimental protocol for wear testing showing four loading stages and scanning points

4.2.5.7 Post-Wear and Tibia-Only Scanning

Following each 250,000-cycle loading stage, the tibia and femur were redigitized to assess any kinematic changes during testing and the potted tibia was scanned via the 3D optical scanner similar to the pre-wear scanning procedure mentioned previously. This was done to generate the post-wear tibia-meniscus (Scan 2) **(Figure 31B)**. Once all four loading stages and post-wear scans were complete, both the lateral and medial meniscus were dissected from the tibia bone. The tibia-only was then scanned in the same manner as the pre- and post-wear procedures to generate Scan 3 **(Figure 31B)**.

4.2.5.8 Volumetric Wear and Stiffness Analysis

The pre-wear, four post-wear, and tibia-only renderings were analyzed in CloudCompare via the procedure outlined in section 4.2.4, with additional alignment steps. Fine alignment was performed by selecting points along the medial and lateral meniscus

ridge to align the tibia-only with pre- and post-wear tibia-menisci renderings. This was done under the assumption that the outer ridge did not deform nor shift during mechanical testing. CGS was then preformed to isolate each meniscus. Excess soft tissue on the medial and lateral meniscus renderings was then systematically removed by applying a defined snipping pattern, thus ensuring that each meniscus had the same amount of excess material removed.

The amount of volumetric loss due to tribological behavior (in terms of wear and deformation) was recorded as V_{wear} (mm^3). The overall stiffness of the meniscus structure was analyzed from Instron loading output. The axial stiffness was calculated from axial force and displacement data (N/mm) while the torsional stiffness was obtained from torsion and rotation data (Nm/deg).

4.2.6 Statistical Analysis

A one-way ANOVA test was performed to detect differences in average absolute percentage error between the six defect depths for the simple surrogate model. The effect of defect wear depth and meniscus type (medial or lateral) on the error in measuring volumetric wear in the complex surrogate model was assessed using MANOVA. For both ANOVA and MANOVA analyses, a Bonferroni or Games-Howell post-hoc test was performed for pairwise comparison dependent on variance homogeneity. Significance was set at $p<0.05$ for all statistical analyzes. Statistical software SPSS (IBM v26.0) was utilized for all data analysis. Data are reported as mean ± standard error, unless otherwise stated.

4.3 Results

4.3.1 Simple Surrogate Model: Geometric Blocks

The CGS methodology resulted in 3D renderings that closely resemble that of the real-life geometric blocks **(Figure 35A)**. The magnitude of the defect depths was found to have a significant effect on the absolute mean percentage error. As the defect depth decreased, the error was found to increase significantly (p=0.001). The average accuracy of the methodology when measuring all defect volumes for the blocks was 4.50 ± 4.79 mm^3. The largest defect, 0.15-in, produced an average volumetric percentage error of 0.46±0.1% while the smallest defect, 0.001-in, resulted in an error of 183 ± 3.4%. Intermediate defect blocks showed errors less than 25% with an average error of 13.0 ± 8.6% **(Figure 35B).** Significant difference was found between the 0.15-in defect and the 0.05, 0.005, and 0.002-in defects (p= 0.043, p=0.016, and p=0.042 respectively).

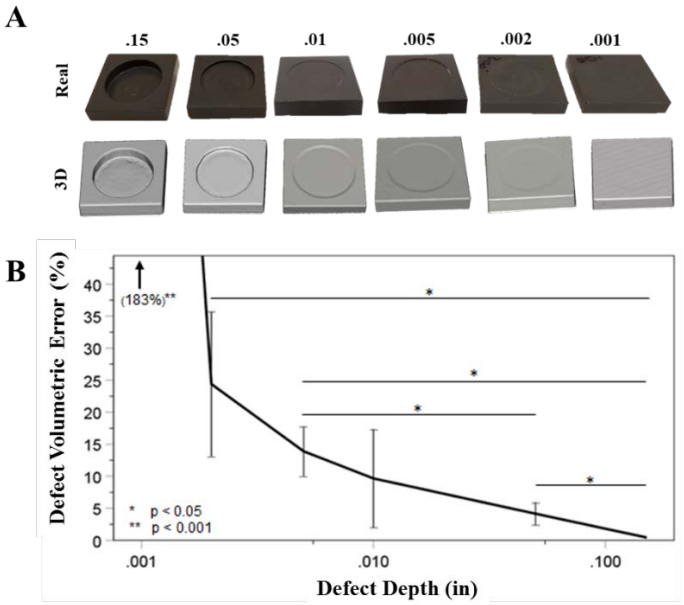

Figure 35. Simple Surrogate Model: Geometric Blocks A) visualization of all defect depths with real-life blocks shown in black while 3D renderings are in gray. B) Percentage error between known and experimental block defect volume increases as defect depth decreases. ** = greater error than all other defect depths (p < 0.001).

4.3.2 Complex Surrogate: Menisci & Tibia Replicas

The defect patterns of the replica menisci were successfully visualized with the 3D optical scanner. The color map indicates the ability of the software to properly align the non-defect control (green) to the defect (blue) in order to isolate the defect entirely while still preserving detail **(Figure 36A)**. The average accuracy of the methodology when measuring all defect volumes for the replica medial and lateral menisci was 10.2 ± 7.13 mm^3 and 8.14 ± 5.68 mm^3, respectively. The corresponding average absolute percentage errors in quantifying defect volume were 14.5 ± 12.1% and 16.7 ± 14.1% for medial and lateral meniscus, respectively. When preforming CGS between the tibia-meniscus and tibia only, the isolated menisci yield errors of <6%. Significant difference was reported for the lateral meniscus between the 0.05 in and control depths ($p=0.033$) while no significance was found for the medial meniscus ($p>0.05$) **(Figure 36B)**. Data from isolating the defect through CGS illustrate that error increased as defect depth decreased for each meniscus ($p<0.05$). Significance was found between the 0.005 in defect depth and all other defect depths for both the lateral and medial meniscus ($p<0.05$) Further significance was found between medial meniscus defect depths of 0.05 in and 0.001 in ($p=0.01$), 0.01 in and 0.025 in ($p=0.022$) **(Figure 36C).**

To test the practicality of the CGS method, the method was compared to a simple volume difference calculation that calculated the meniscus volume from numeric subtraction of tibia-only from tibia-meniscus volume. The defect was then numerically calculated from subtracting the pre-meniscus from post-meniscus. The absolute mean percent error was found to be significantly different between this volume difference

calculation and CGS method (p=0.011). Volume difference produced average percentage errors 2.2x greater than CGS, therefore indicating the preference to use the CGS method.

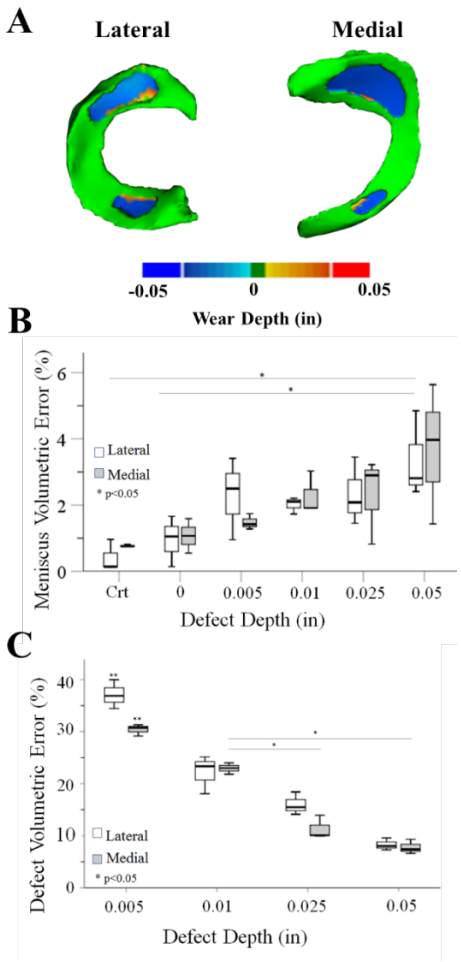

Figure 36. Complex Surrogate Model: Menisci & Tibia Replicas A) Colorimetric heat map of 0.05-in defect (blue) aligned to the control defect (green) shows tight alignment for the CGS method, B) Medial and lateral menisci volumetric error using the CGS method results in errors of less than 6% percent, C) CGS defect volumetric error increases as defect depth decreases for both lateral and medial menisci (p<0.05). ** = greater error than all other defect depths (p < 0.05).

4.3.3 Instron Loading Profile

Axial loading with maximum and minimum forces of 2.4kN and 0.2kN, respectively, remained constant and corresponded to ISO targets throughout the 1 million cycles **(Figure 37 A)**. As shown in **Table 2**, average peak axial loading and rotation was

within 3.3 ± 4.0% and 292 ± 353% of the targeted target values, respectfully. The amplitude of tibial rotation increased for every 250,000 cycles yet was outside of the ISO set maximum and minimum targets **(Figure 37B).** Displacement increased from 250,000 to 500,000 cycles however tended to decrease in later cycles **(Figure 37C)**. Torque increased throughout all loading stages resulting in the highest torque during the fourth loading stage, Axial and torsional stiffness were calculated from the Instron data to be 23.63.88 N/mm and 1.83±2.53 N/deg, respectively.

Table 2. Errors in reaching ISO peak maximum and minimum targets for axial loading (2.4 kN and 0.2 kN) and rotation (0.55 deg and -0.55 deg)

	250K Cycles		500K Cycles		750K Cycles		1000K Cycles	
	Peak Max	Peak Min	Peak Max	Peak Min	Peak Max	Peak Min	Peak Max	Peak Min
Axial Force Error (%)	0.31	6.21	0.59	2.1	0.26	5.54	0.26	11.3
Rotation Angle Error (%)	7.3	-14.5	116	-131	255	-220	315	-276

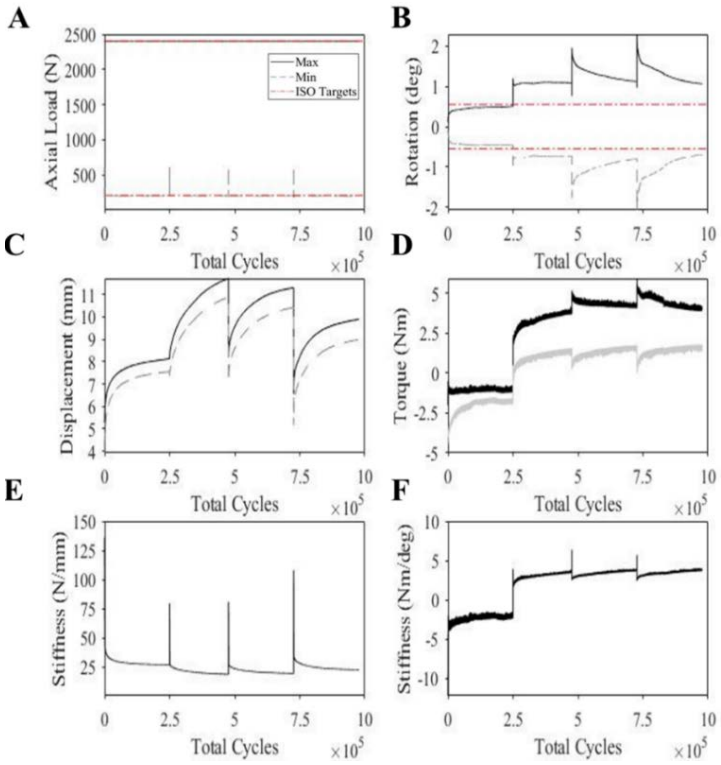

Figure 37. Instron data throughout 1 million cycles: A) Axial loading is within range of ISO targets while B) rotation strays away from the targets after the first loading stage. C) Displacement, D) torque, E) axial stiffness, and F) torsional Stiffness are dependent upon the set axial and rotational parameters.

4.3.4 In Vitro Human Application

The tibia-meniscus was inspected for tribological behavior in terms of wear and deformation following each loading stage. Prominent discoloration in the tissue is seen in both lateral and medial meniscus for all four loading stages **(Figure 38A)**. The tibia-only showed extensive damage to the anterolateral region of the tibial surface in the form of cracking along the inner region of the tibia surface **(Figure 38A)**. Throughout loading, the tibial surface became more prominent and the inner peripheral regions of both lateral and medial meniscus appeared to recede **(Figure 38B)**.

The CGS method yielded isolated renderings of the lateral and medial meniscus **(Figure 39A)** that were further analyzed to quantify the volume of each whole meniscus. The lateral and medial meniscus volume decreased as the number of cycles increased

(Figure 39B). The first 250,000 cycle loading stage induced the greatest decrease in whole lateral meniscus volume from 3282.83 mm^3 to 1928.18 mm^3, while the medial meniscus experienced the greatest amount of volume change from the second and third loading stages with volumes of 2803.6 mm^3 and 2450.9 mm^3, respectively.

The CGS method isolated the wear and deformation and illustrated that as the cycles increased, the defect volume increased, with the exception of the third loading stage **(Figure 39C).** During this loading stage, the defect volume for both lateral and medial meniscus (1131.04 mm^3 and 1723.96 mm^3, respectively) was less than the previous loading stages (1132.09 mm^3 and 1767.93 mm^3, respectively).

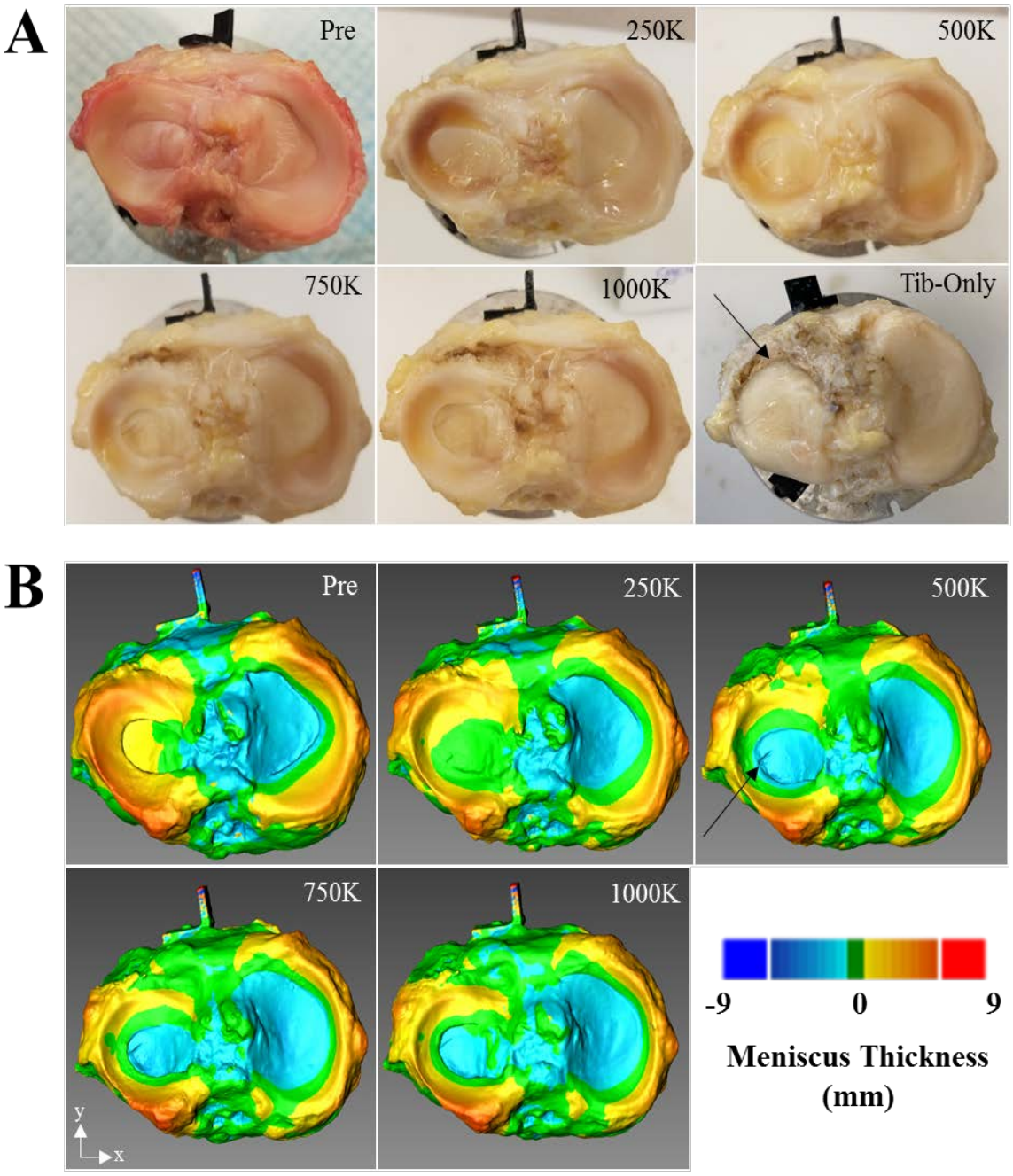

Figure 38. Wear and deformation are visualized in the tibia-meniscus subjected to 1 million cycles: A) images of pre- and post-wear show discolored tissue while B) heat map comparisons of tibia-only to pre- and post-wear illustrate prominent deformation.

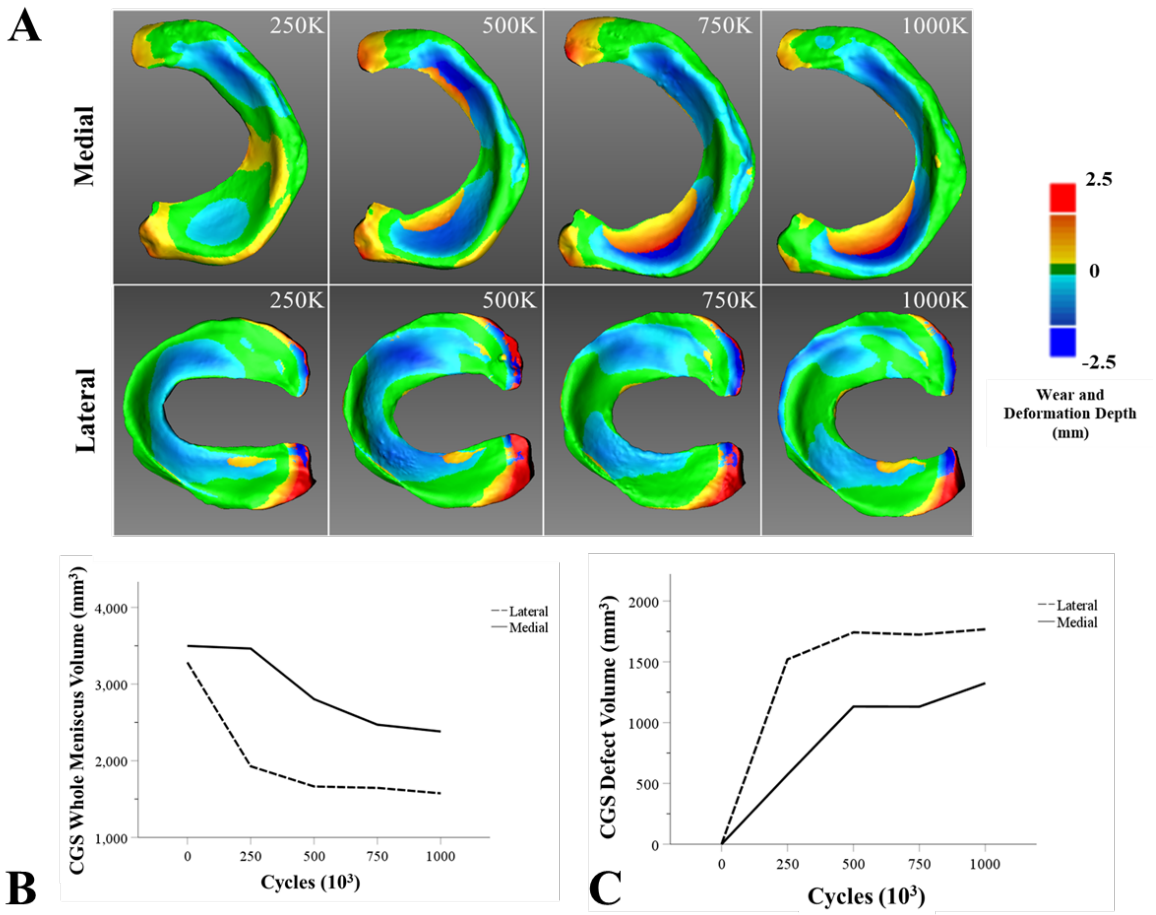

Figure 39. Wear and deformation analysis: A) Colorimetric heat maps showing differences between pre- and post-wear medial and lateral meniscus. Higher wear and deformation are indicated by darker blue regions within each meniscus. The CGS method illustrates B) the volume for each meniscus decreases while C) the wear and deformation volume increases as the number of cycles increases.

4.4 Discussion

Characterizing meniscus wear behavior is vital to determine strategies for preventing meniscus degeneration and to identify the best course of treatment for degenerative meniscus complications. This study has therefore developed and verified a novel method to be used with 3D optical scanning techniques to quantify and visualize wear and deformation in whole human meniscus tissue. This is also the first study to analyze in vitro wear and deformation of whole human meniscus subjected to physiological loading conditions.

To determine the accuracy of this novel method, we developed two surrogate models that had known wear volumes. The simple surrogate model provided a best-case scenario when using the 3D scanner and CGS method to detect volumetric defects. Based on this analysis, we found that the developed method is capable of detecting volumetric changes in simple geometry of 0.4 cm^3, roughly the size of a pea [85] with less than 5% error **(Figure 35B)**. However, as the object of interest became more complex, as seen with the surrogates of menisci replicas, volumetric percentage errors increased nearly two-fold, thus suggesting our method is influenced by object geometry. The most likely reason for this increase in error is due to concave regions in the complex geometry which lead to artifacts in the 3D renderings due to poorly reflected light. Therefore, in complex geometry the method is capable of detecting wear the size of a pea with less than 8% error **(Figure 36C)**. Additionally, both surrogates were able to accurately measure the pre-wear volume of the whole meniscus surrogate with less than 6% error **(Figure 36B)**. The results from the surrogate models demonstrate that 3D optical scanning and CGS analysis can provide an accurate method for measuring whole human meniscus volume and characterizing volumetric changes due to global wear and deformation.

While several studies have measured volumetric wear loss in joint prosthetic materials [46,48,78,86,87], error verification of their methods is absent; therefore, we are unable directly compare our accuracy results with these prior studies. Although a recent study by Bowland et al. also neglects method verification, it is the closest study comparable to our own current work. This study utilized a knee simulator and optical profilometry to analyze tribological performance of osteochondral grafts within a whole porcine knee model [75]. This work demonstrated the capability of optical profilometry to measure

volumetric wear, deformation, and damage on the opposing meniscal surfaces to the medial femoral condyle as a result of mechanical joint stimulation. However, the method used by Bowland et al. was limited to only detecting localized focal defects through topographical data [6]. Therefore, while meniscus volume loss was measured, it was only representative of localized focal defects and did not account for defects that may have occurred in other regions of the meniscus.

Our study was able to successfully detect and isolate global wear and deformation of the whole human meniscus using the developed method. This study demonstrated interesting findings for the in vitro wear assessment of the whole human meniscus. *Firstly*, throughout 1 million cycles of loading, it can be seen that the menisci were heavily impacted by the mechanical loading. This is most clearly visualized from the colorimetric map in **Figure 38B** showing a prominent reduction of yellow hue around both lateral and medial meniscus from one loading stage to the next. This therefore indicates a decrease in meniscus thickness and suggests that the meniscus tissue deformed during loading. *Secondly*, the tibial surface became more prominent and the inner peripheral region of both lateral and medial meniscus began to recede throughout loading stages **(Figure 38)**. Additionally, it was found that the reduction in protective coverage of the articular surface by the menisci led to cracks within the lateral region of the tibial surface, as indicated by the arrow in **Figure 38B**. *Thirdly*, colorimetric mapping enabled the visualization of high wear and deformation regions throughout the meniscus structure. From **Figure 39A**, we can see that the depth of wear and deformation is most prominent in the anterior and posterior regions of the medial meniscus, as indicated by the dark blue coloring. The lateral meniscus appears to show the greatest wear and deformation depth in the middle regions.

Fourthly, volume loss may have been a result of material wear, deformation, or a combination of both wear and deformation. When subtracting the post-wear meniscus from the pre-wear meniscus, we would expect to isolate the prominent regions of wear indicated by the heat map patterns in **Figure 39A**. However, due to the menisci being compressed, the geometry of each meniscus deformed from pre- to post-wear time points, resulting in gross shape differences. The relative position of the post-wear meniscus was more variable than the pre-wear meniscus; therefore, the assumption had to be made that the ridges of the pre- and post-wear menisci did not deform. With this assumption, the pre- and post-wear meniscus could be aligned; however, when alignment was performed, complete overlap in meniscus geometry was not achieved due to the presence of deformation. When CGS was performed, only the common geometry between the two models was subtracted, thus isolating wear and leaving any post-wear material that did not conform to the pre-wear meniscus shape. Therefore, this left-over material may have represented deformation and contributed to the final measure of meniscus volume loss between the pre- and post-wear time points. However, the distinction between whether or not material wear or deformation fully or partially contributed to volume loss could not be distinguished. Thus, the term "wear" was reclassified in terms of "wear and deformation". Wear and deformation volumes for the medial and lateral meniscus were therefore shown to increase throughout loading stages with the lateral meniscus experiencing 25.1% higher wear and deformation volume than the medial meniscus **(Figure 39C)**. *Lastly*, the developed method yields meniscus volumes that are directly comparable to known human meniscus volume. The pre-wear medial and lateral meniscus volumes obtained from CGS were found to be 3496 mm^3 and 3283 mm^3, respectively. In a healthy knee, menisci volumes of 3041 ± 43 mm^3

and 3067 ± 71 mm^3 for the medial and lateral meniscus have been reported from water volume displacement techniques [87]. While the experimental volumes are slightly greater than these known reported values, this indicates that the method can successfully represent whole human meniscus volume.

The 3D scanner method can be compared to additional methods commonly used to measure wear in joint prosthetic material. Many studies [46–48,77] have utilized gravimetrics analysis for measuring structural wear via mass loss in joint replacement materials. However, for soft tissue, this method is not applicable as it requires vacuum desiccation at various time points that would be unsuitable for hydrated soft tissues. Moreover, gravimetrics does not allow for the detection and visualization of regional wear patterns, which is crucial in identifying regions within meniscus that are more susceptible to wear and deformation. A study by Elsner et al. utilized micro-CT analysis to measure volumetric wear changes in synthetic meniscus inserts. While this method was found to be capable of detecting wear patterns and quantifying volumetric wear changes in synthetic material, it is limited in terms of high run time and equipment cost. A micro-CT scan can take 95 min to 4 h to complete a quality 3D image [47,87], while the 3D scanning method took an average of 45 min to complete a high-quality 3D model and perform CGS. Additionally, micro-CT scanning equipment can cost up to 15 times as much as the 3D optical scanning system used in the present study, which can be purchased for between $15,000 and $25,000 [47]. Furthermore, MRI scanning techniques have been found to successfully measure in vivo volume of soft tissues meniscus [87]. However, MRI lacks sufficient imaging resolution to preserve microscale detail and detect volumetric changes within the tissue. Therefore, the practical advantage of 3D optical scanning and the

developed method with respect to time, cost, and most importantly, the ability to visualize and quantify meniscus wear, makes this a study promising for future evaluations of soft tissue wear and deformation.

There were several notable limitations present within this study. Firstly, we only tested one human cadaveric knee. While a single test was sufficient to demonstrate our novel technique, more test would clearly be needed to characterize meniscus wear and deformation behavior for specific loading conditions and anatomical factors. Secondly, during dissection, many of the menisci soft tissue attachments had to be removed in order to comply with the testing setup and methodology. Therefore, the normal alignment and attachments of the soft tissue structures of the knee joint were not reproducible. Thirdly, the amplitude of tibial rotation was outside of the ISO set maximum and minimum targets. This can be attributed to a potential control error within the Instron software since the set amplitude should have stayed consistent throughout the 1 million cycles. Lastly, the presence of deformation influenced the developed method when aligning models and performing CGS to isolate meniscus defects. As the menisci continued to deform during cyclic loading cycles, the assumption had to be made that the outer ridge of the menisci did not move. This assumption allowed us to apply fine alignment techniques to manually align the pre- and post-wear menisci by selecting common points along the ridge to serve as reference alignment markers. From **Figure 39A**, we can see that this alignment along the ridge resulted in a relatively tight alignment, as indicated by the green coloring. However, there is evidence that this alignment was not completely exact due to the presence of light blue coloring along both lateral and medial meniscus ridges. If the meniscal ridges did not move nor deform during wear testing, then we would expect to strictly see green coloring

along the ridge. Therefore, this assumption may not have been entirely true, thereby resulting in skewed alignment of pre- and post-wear menisci leading to greater wear and deformation volumes.

4.5 Conclusion

The 3D optical scanning method developed in this study (CGS) can now be used to assess anatomical and physical factors that may increase the risk of wear and injury in meniscus. For example, future experiments are planned to use this method to assess the effect of specific physiological loading activities on regional wear patterns in cadaveric meniscus. In summary, this study has developed and validated a new technique to measure soft tissue wear in intact joints that has the potential to advance fundamental knowledge of wear and deformation behavior in meniscus, as well as other articulating soft tissues (e.g. intervertebral disc and articular cartilage).

CHAPTER FIVE: PROJECT CONCLUSIONS

5.1 Summary

The primary goal of this research was to develop and verify an in vitro methodology to quantify and visualize wear in meniscus tissue. Prior to human meniscus tissue wear testing, the developed common geometry subtraction (CGS) method was verified through simple and complex geometry surrogates. Next, the CGS method was used to quantify wear and deformation in whole human cadaveric meniscus tissue.

Key conclusions include:

- A Common Geometry Subtraction (CGS) technique was developed using open-sourced software programs, MeshLab and CloudCompare, to accurately measure volumetric changes.
- A kinematic knee fixture capable of allowing six degrees of adjustment was designed and fabricated to hold the tibia and femur in placed during mechanical wear testing in accordance with ISO 14243-3.
- The novel imaging method has an inherent error of <5% when measuring defect volumes >0.4 cm^3. This error increases two-fold for complex geometry.
- Overall whole meniscus volume reductions of 52.0% and 31.9% were seen for the lateral and medial meniscus, respectively, when applying 1 million cycles of loading at 45% of the gait cycle.
- Generating colorimetric maps enabled the detection and visualization of wear and deformation

- Defects due to wear and deformation in whole human meniscus were isolated and volumetrically quantified for the first time, or to our knowledge, any whole soft tissue structure.

5.2 Limitations

This study consists of many limitations. First, this study utilized a sample size of only one cadaveric knee. This small sample size does not account for possible anatomic variations between different specimens nor does it allow for statistical analysis to be performed. Therefore, we are unable to determine if there is statistical significance between meniscus type and number of loading cycles. An increase in sample size would allow for a more representative study. Second, when dissecting the knee joint, important meniscal attachments, such as the MCL, meniscofemoral ligaments, and ligaments of Humphrey and Winslow, must be sacrificed for the testing setup and methodology. This results in a knee joint environment that is not fully representative of natural meniscus attachments and may disrupt joint kinematics. Third, replicating the natural kinematic alignment of the knee joint during potting was ill achieved. The digitization process was highly sensitive when hitting the marked boney landmarks. If the digitizer did not hit the marker target in the exact same way and location during digitizing, the kinematic rotations and translations were skewed. This could have greatly influence kinematic positioning of the bones during wear testing. Fourth, the Instron loading profile did not hit the ISO specified targets (section 4.3.3) which resulted in the misrepresentation of loading at 45% of the gait cycle. Additionally, during the second 250,000 cycle loading stage, the limits on the Instron were tripped and the wear test stopped twice. Both times the Instron and loading profile were reset and the test was allowed to run until completion. This event may have contributed to the control error in

tibial rotation. Fifth, the CGS method experienced difficulties in aligning the soft tissue menisci due to a large degree of deformation. Therefore, as the menisci continued to deform during cyclic loading cycles, the assumption had to be made that the outer ridge of the menisci did not move. This may not be entirely true and therefore may have resulted in inadequate alignment of pre- and post-wear menisci.

5.3 Future Work

A proposed study has been identified to further expand this work to examine the cause-effect relationship between specific physiological activities and the mechanical wear responses of whole human meniscus. Based on the initial work done within the present study, it is hypothesized that torsional loading at high flexion angles will promote fibrous tissue breakdown and will lead to greater wear rates.

The first aim of this proposed study is to quantify volumetric meniscal wear associated with physiological activity. Previous studies have shown that contact stresses within meniscus tissue increase with greater flexion angles, leading to the potential to influence wear rates [36,88]. Additionally, wear debris in polyethylene knee replacement bearings has been found to increase under increasing internal-external rotation [89]. Therefore, the flexion angle of the knee joint and the amount of torsional rotation may be contributing factors to meniscal tissue wear. Human gait data for three different activities (normal gait, deep-squat, and pivot) obtained from the Center for Orthopedic and Biomechanics Research lab at Boise State University (BSU) can be used to generate kinematic profiles. These physiological activities have been identified from previous gait studies to produce high degrees of flexion and rotation with increased torsional loading

[90,91]. Using the acquired kinematic information, knee simulator that was previously built will be modified to accommodate these different loading conditions.

Nine cadaveric knees will be split into three loading groups based on the physiological activities. Similar to the present study, all soft tissue from the knee joint will be removed except for the menisci and select attachments. The femur and tibia-meniscus will be cemented in the custom knee simulator and submerged in 37C bovine synovial fluid. Each specimen will be loaded into the Instron and subjected to the proper kinematic loading profile at 2Hz for four loading stages of 250,000 cycles, resulting in a total of 1 million loading cycles.

Using the 3D optical scanner and developed CGS analysis techniques, 3D renderings of the meniscus will be created. Each model will follow the experimental design protocol and will be generated by aligning 8 scans at 45-degree increments, allowing for a full 360-degree view of the tibia-meniscus. During wear testing, post-wear scans will be taken after every 250,000 cycles resulting in a total of four post-wear renderings. To calculate the volumetric wear, models will be analyzed using open-source software (MeshLab, CloudCompare). If wear is not present after 1 million cycles, an additional four sets of 250,000 cycles will be done to determine time points for wear development. Following testing, the composition of the meniscal fibrous matrix will be analyzed through scanning electron microscopy and biochemical assays.

The second aim of this proposed study will be to develop and implement a computational weal model. In collaboration with the Computational Biosciences Laboratory at BSU, a subject-specific finite element models of the knee (Abaqus/Explicit) using established methods [92] will be created. Archard’s wear law will then be used to

predict the total volume of wear debris produced from the physiological loads. To calibrate the model parameters, the predicted volumetric wear will be compared to the actual volumetric wear measured in our experiments at two time points (500k, 1 million cycles), and model validation will be performed by comparing model predictions versus experimental results for the other two time points (250k, 750k cycles).

This proposed research will yield extensive quantitative understanding of meniscus wear and advance fundamental knowledge of the etiology of degenerative wear within meniscus and other articulating soft tissue structures. Additionally, this study will provide comprehensive visualization and identification of global defects within the meniscus, allowing for the detection of morphological regions that are more prone to wear. These insights could aid in the evolution of tissue engineering techniques for durable replacement tissue [93]. Lastly, the validation of a wear model using finite elements will advance knowledge in meniscus pathomechanics and will enable researchers to predict wear behavior for a broad range of physical activities and anatomical variations.

To account for limitations in the current study, the following will be done:

1. The sample size will be increase to nine in order to compensate for anatomical variations between specimens.
2. Removal of meniscal attachments will remain a limitation due to the study setup.
3. The kinematic alignment will be adjusted to include better positioning of boney landmark markers to reduce error when digitizing points.
4. The Instron data will be monitored during testing and the limits of the test will be adjusted to ensure an error warning is thrown if the rotation is out of range.

5. The CGS method for isolating meniscus wear and deformation can be improved by adding additional markers on the tibia as well as the outer ridge of the menisci to aide in fine alignment.

REFERENCES

[1] M. Morlock, E. Schneider, A. Bluhm, M. Vollmer, G. Bergmann, V. Müller, M. Honl, Duration and frequency of every day activities in total hip patients, in: J. Biomech., Elsevier, 2001: pp. 873–881. https://doi.org/10.1016/S0021-9290(01)00035-5.

[2] A.J.S. Fox, A. Bedi, S.A. Rodeo, The Basic Science of Human Knee Menisci: Structure, Composition, and Function, Sports Health. 4 (2012) 340–351. https://doi.org/10.1177/1941738111429419.

[3] B. Gelbart, P. Firer, Meniscus injuries: Where do we stand? BR Gelbart P Firer Orthopaedic Surgeon, Netcare Linksfield Clinic, Orange Grove, Johannesburg; Honorary Consultant, Charlotte Maxeke Johannesburg Hospital Soft Tissue Knee Clinic, 2009.

[4] R. Howell, N.S. Kumar, N. Patel, J. Tom, Degenerative meniscus: Pathogenesis, diagnosis, and treatment options, World J. Orthop. 5 (2014) 597–602. https://doi.org/10.5312/wjo.v5.i5.597.

[5] E.A. Makris, P. Hadidi, K.A. Athanasiou, The knee meniscus: Structure-function, pathophysiology, current repair techniques, and prospects for regeneration, Biomaterials. 32 (2011) 7411–7431. https://doi.org/10.1016/j.biomaterials.2011.06.037.

[6] P. Bowland, Biotribology of Osteochondral Grafts in the Knee, 2016.

[7] K.M. Fischenich, J. Lewis, K.A. Kindsfater, T.S. Bailey, T.L. Haut Donahue, Effects of degeneration on the compressive and tensile properties of human meniscus, J. Biomech. 48 (2015) 1407–1411. https://doi.org/10.1016/j.jbiomech.2015.02.042.

[8] J. Herwig, E. Egner, E. Buddecke, Chemical changes of human knee joint menisci in various stages of degeneration, 1984. https://www.ncbi.nlm.nih.gov/pmc/articles/PMC1001426/pdf/annrheumd00253-0103.pdf (accessed July 8, 2019).

[9] A.J. Rao, B.J. Erickson, G.L. Cvetanovich, A.B. Yanke, B.R. Bach, B.J. Cole, The Meniscus-Deficient Knee: Biomechanics, Evaluation, and Treatment Options, Orthop. J. Sport. Med. 3 (2015). https://doi.org/10.1177/2325967115611386.

[10] B.A.M. Snoeker, E.W.P. Bakker, C.A.T. Kegel, C. Lucas, Risk factors for meniscal tears: A systematic review including meta-analysis, J. Orthop. Sports Phys. Ther. 43 (2013) 352–367. https://doi.org/10.2519/jospt.2013.4295.

[11] M. Englund, A. Guermazi, D. Gale, D.J. Hunter, P. Aliabadi, M. Clancy, D.T. Felson, Incidental meniscal findings on knee MRI in middle-aged and elderly persons, N. Engl. J. Med. 359 (2008) 1108–1115. https://doi.org/10.1056/NEJMoa0800777.

[12] V. Campanelli, S.M. Howell, M.L. Hull, Accuracy evaluation of a lower-cost and four higher-cost laser scanners, J. Biomech. 49 (2016) 127–131. https://doi.org/10.1016/j.jbiomech.2015.11.015.

[13] M. Englund, F.W. Roemer, D. Hayashi, M.D. Crema, A. Guermazi, Meniscus pathology, osteoarthritis and the treatment controversy, Nat. Rev. Rheumatol. 8 (2012) 412–419. https://doi.org/10.1038/nrrheum.2012.69.

[14] M.E. Baratz, F.H. Fu, R. Mengato, Meniscal tears: the effect of meniscectomy and of repair on intraarticular contact areas and stress in the human knee. A preliminary report., Am. J. Sports Med. 14 (1986) 270–5. https://doi.org/10.1177/036354658601400405.

[15] J.N. Katz, R.H. Brophy, C.E. Chaisson, L. De Chaves, B.J. Cole, D.L. Dahm, L.A. Donnell-Fink, A. Guermazi, A.K. Haas, M.H. Jones, B.A. Levy, L.A. Mandl, S.D. Martin, R.G. Marx, A. Miniaci, M.J. Matava, J. Palmisano, E.K. Reinke, B.E. Richardson, B.N. Rome, C.E. Safran-Norton, D.J. Skoniecki, D.H. Solomon, M. V Smith, K.P. Spindler, M.J. Stuart, J. Wright, R.W. Wright, E. Losina, F. Brigham, J.N.K. Women's Hospital, B. University, W. University, S. Louis, Surgery versus Physical Therapy for a Meniscal Tear and Osteoarthritis A bs t r ac t, N Engl j Med. 18 (2013) 1675–84. https://doi.org/10.1056/NEJMoa1301408.

[16] N.J. Kise, M.A. Risberg, S. Stensrud, J. Ranstam, L. Engebretsen, E.M. Roos, Exercise therapy versus arthroscopic partial meniscectomy for degenerative meniscal tear in middle aged patients: Randomised controlled trial with two year follow-up, BMJ. 354 (2016). https://doi.org/10.1136/bmj.i3740.

[17] D. Bartel, D. Davy, T.M. Keaveny, Orthopaedic Biomechanics: Mechanics and Design in Musculoskeletal Systems, 2006.

[18] D.D. D'Lima, S. Patil, N. Steklov, S. Chien, C.W. Colwell, In vivo knee moments and shear after total knee arthroplasty, J. Biomech. 40 (2007) S11–S17. https://doi.org/10.1016/j.jbiomech.2007.03.004.

[19] K.M. Steele, M.S. DeMers, M.H. Schwartz, S.L. Delp, Compressive tibiofemoral force during crouch gait, Gait Posture. 35 (2012) 556–560. https://doi.org/10.1016/j.gaitpost.2011.11.023.

[20] G. Verberne, Y. Merkher, G. Halperin, A. Maroudas, I. Etsion, Techniques for assessment of wear between human cartilage surfaces, Wear. (2009). https://doi.org/10.1016/j.wear.2009.03.042.

[21] F. Flandry, G. Hommel, Normal Anatomy and Biomechanics of the Knee, 2011. www.sportsmedarthro.com (accessed October 15, 2020).

[22] M. Marieswaran, I. Jain, B. Garg, V. Sharma, D. Kalyanasundaram, A Review on Biomechanics of Anterior Cruciate Ligament and Materials for Reconstruction, (2018). https://doi.org/10.1155/2018/4657824.

[23] E. Vaienti, G. Scita, F. Ceccarelli, F. Pogliacomi, Understanding the human knee and its relationship to total knee replacement, Acta Biomed. 88 (2017) 6–16. https://doi.org/10.23750/abm.v88i2-S.6507.

[24] J. Perry, J.M. Burnfield, Gait Analysis: Normal and Pathological Function, 2010. http://www.jssm.org (accessed October 15, 2020).

[25] J. Dargel, M. Gotter, K. Mader, D. Pennig, J. Koebke, R. Schmidt-Wiethoff, Biomechanics of the anterior cruciate ligament and implications for surgical reconstruction, Strateg. Trauma Limb Reconstr. 2 (2007) 1–12. https://doi.org/10.1007/s11751-007-0016-6.

[26] S.L.Y. Woo, S.D. Abramowitch, R. Kilger, R. Liang, Biomechanics of knee ligaments: Injury, healing, and repair, J. Biomech. 39 (2006) 1–20. https://doi.org/10.1016/j.jbiomech.2004.10.025.

[27] U. Naqvi, A. l. Sherman, Medial Collateral Ligament (MCL) Knee Injuries, StatPearls Publishing, 2020. http://www.ncbi.nlm.nih.gov/pubmed/28613747 (accessed October 15, 2020).

[28] R.J. Yaras, N. O'Neill, A.M. Yaish, Lateral Collateral Ligament (LCL) Knee Injuries, StatPearls Publishing, 2020. http://www.ncbi.nlm.nih.gov/pubmed/32809682 (accessed October 15, 2020).

[29] J.J. Cherian, B.H. Kapadia, S. Banerjee, J.J. Jauregui, K. Issa, M.A. Mont, Mechanical, anatomical, and kinematic axis in TKA: Concepts and practical applications, in: Curr. Rev. Musculoskelet. Med., Humana Press Inc., 2014: pp. 89–95. https://doi.org/10.1007/s12178-014-9218-y.

[30] C.F. Luo, Reference axes for reconstruction of the knee, Knee. 11 (2004) 251–257. https://doi.org/10.1016/j.knee.2004.03.003.

[31] R. Shenoy, P.S. Pastides, D. Nathwani, (iii) Biomechanics of the knee and TKR, 2013. https://doi.org/10.1016/j.mporth.2013.10.003.

[32] E.S. Grood, W.J. Suntay, A Joint Coordinate System for the Clinical Description of Three-Dimensional Motions: Application to the Knee, J. Biomech. Eng. 105 (1983) 136. https://doi.org/10.1115/1.3138397.

[33] S.D. Masouros, A.M.J. Bull, A.A. Amis, (i) Biomechanics of the knee joint, Orthop. Trauma. 24 (2010) 84–91. https://doi.org/10.1016/j.mporth.2010.03.005.

[34] P. Johal, A. Williams, P. Wragg, D. Hunt, W. Gedroyc, Tibio-femoral movement in the living knee. A study of weight bearing and non-weight bearing knee kinematics using “interventional” MRI, J. Biomech. 38 (2005) 269–276. https://doi.org/10.1016/j.jbiomech.2004.02.008.

[35] C.R. Clark, J. Ogden, A Development of the menisci of the human knee joint. Morphological changes and their potential role in childhood meniscal injury, J. Bone Jt. Surg. 65 (1983) 538–547. https://doi.org/10.2106/JBJS.L.01195.

[36] K. Zhang, L. Li, L. Yang, J. Shi, L. Zhu, H. Liang, X. Wang, X. Yang, Q. Jiang, Effect of degenerative and radial tears of the meniscus and resultant meniscectomy on the knee joint: a finite element analysis, J. Orthop. Transl. 18 (2019) 20–31. https://doi.org/10.1016/j.jot.2018.12.004.

[37] A. Tsujii, N. Nakamura, S. Horibe, Age-related changes in the knee meniscus, Knee. 24 (2017) 1262–1270. https://doi.org/10.1016/j.knee.2017.08.001.

[38] J.C. Gray, Neural and vascular anatomy of the menisci of the human knee, J. Orthop. Sports Phys. Ther. 29 (1999) 23–30. https://doi.org/10.2519/jospt.1999.29.1.23.

[39] R. Bayer, Mechanical Wear Fundamentals and Testing, Revised and Expanded, 2004. https://doi.org/10.1201/9780203021798.

[40] Z.M. Jin, M. Stone, E. Ingham, J. Fisher, (v) Biotribology, in: Curr. Orthop., Churchill Livingstone, 2006: pp. 32–40. https://doi.org/10.1016/j.cuor.2005.09.005.

[41] S. Affatato, D. Brando, Introduction to wear phenomena of orthopaedic implants, in: Wear Orthop. Implant. Artif. Joints, Elsevier, 2013: pp. 3–26. https://doi.org/10.1533/9780857096128.1.3.

[42] T. Yamamoto, Wear mechanism based on adhesion, (n.d.). https://archive.org/details/nasa_techdoc_19820024861/page/n15/mode/2up (accessed November 3, 2020).

[43] M.C. Valigi, S. Logozzo, S. Affatato, New challenges in tribology: Wear assessment using 3D optical scanners, Materials (Basel). 10 (2017). https://doi.org/10.3390/ma10050548.

[44] ISO 14242-2, International Standard 14242-2: Implants for surgery —Wear of total hip-joint prostheses — Part 2: Methods of measurement, 61010-1 © Iec2001. 2006 (2006) 13.

[45] A.L. Galvin, L. Kang, I. Udofia, L.M. Jennings, H.M.J. McEwen, Z. Jin, J. Fisher, Effect of conformity and contact stress on wear in fixed-bearing total knee prostheses, J. Biomech. 42 (2009) 1898–1902. https://doi.org/10.1016/j.jbiomech.2009.05.010.

[46] J.J. Elsner, M. Shemesh, A. Shefy-Peleg, Y. Gabet, E. Zylberberg, E. Linder-Ganz, Quantification of in vitro wear of a synthetic meniscus implant using gravimetric and micro-CT measurements, J. Mech. Behav. Biomed. Mater. 49 (2015) 310–320. https://doi.org/10.1016/j.jmbbm.2015.05.017.

[47] K.A. Hollar, D.S. Ferguson, J.B. Everingham, J.L. Helms, K.J. Warburton, T.J. Lujan, Quantifying wear depth in hip prostheses using a 3D optical scanner, Wear. 394–395 (2018) 195–202. https://doi.org/10.1016/j.wear.2017.10.008.

[48] S. Affatato, A. Leardini, W. Leardini, S. Giannini, M. Viceconti, Meniscal wear at a three-component total ankle prosthesis by a knee joint simulator, J. Biomech. 40 (2007) 1871–1876. https://doi.org/10.1016/j.jbiomech.2006.08.002.

[49] S. Affatato, Tribological interactions of modern biomaterials used in total hip arthroplasty (THA), in: Perspect. Total Hip Arthroplast., Elsevier, 2014: pp. 99–116. https://doi.org/10.1533/9781782420392.2.99.

[50] M. Scott, M. Morrison, S.R. Mishra, S. Jani, Particle analysis for the determination of UHMWPE wear, J. Biomed. Mater. Res. Part B Appl. Biomater. 73B (2005) 325–337. https://doi.org/10.1002/jbm.b.30213.

[51] L. Grillini, S. Affatato, How to measure wear following total hip arthroplasty, HIP Int. 23 (2013) 233–242. https://doi.org/10.5301/hipint.5000003.

[52] L.W. McKeen, Introduction to the Tribology of Fluorocoatings, in: Fluorinated Coatings Finish. Handb., Elsevier, 2016: pp. 277–297. https://doi.org/10.1016/b978-0-323-37126-1.00015-1.

[53] M.M. Blum, T.C. Ovaert, Investigation of friction and surface degradation of innovative boundary lubricant functionalized hydrogel material for use as artificial articular cartilage, Wear. 301 (2013) 201–209. https://doi.org/10.1016/j.wear.2012.11.042.

[54] S.E. Majd, A.I. Rizqy, H.J. Kaper, T.A. Schmidt, R. Kuijer, P.K. Sharma, An in vitro study of cartilage–meniscus tribology to understand the changes caused by a meniscus implant, Colloids Surfaces B Biointerfaces. 155 (2017) 294–303. https://doi.org/10.1016/j.colsurfb.2017.04.034.

[55] L. McCann, E. Ingham, Z. Jin, J. Fisher, An investigation of the effect of conformity of knee hemiarthroplasty designs on contact stress, friction and degeneration of articular cartilage: A tribological study, J. Biomech. 42 (2009) 1326–1331. https://doi.org/10.1016/j.jbiomech.2009.03.028.

[56] L. McCann, E. Ingham, Z. Jin, J. Fisher, Influence of the meniscus on friction and degradation of cartilage in the natural knee joint, Osteoarthr. Cartil. 17 (2009) 995–1000. https://doi.org/10.1016/j.joca.2009.02.012.

[57] L. Shi, V.I. Sikavitsas, A. Striolo, Experimental Friction Coefficients for Bovine Cartilage Measured with a Pin-on-Disk Tribometer: Testing Configuration and Lubricant Effects, (n.d.). https://doi.org/10.1007/s10439-010-0167-3.

[58] Structured Light 3D Scanning: What Is It and How Does It Work? - 3D Insider, (n.d.). https://3dinsider.com/structured-light-3d-scanning/ (accessed November 4, 2020).

[59] The Complete Guide to 3D Scanners using Laser Triangulation - 3Dnatives, (n.d.). https://www.3dnatives.com/en/3d-scanner-laser-triangulation080920174-99/#! (accessed November 4, 2020).

[60] G.A. Idrobo-Pizo, J.M.S.T. Motta, R.C. Sampaio, A calibration method for a laser triangulation scanner mounted on a robot arm for surface mapping, Sensors (Switzerland). 19 (2019). https://doi.org/10.3390/s19081783.

[61] S.C. Park, M. Chang, Reverse engineering with a structured light system, Comput. Ind. Eng. 57 (2009) 1377–1384. https://doi.org/10.1016/j.cie.2009.07.005.

[62] S. Son, H. Park, K.H. Lee, Automated laser scanning system for reverse engineering and inspection, Int. J. Mach. Tools Manuf. 42 (2002) 889–897. https://doi.org/10.1016/S0890-6955(02)00030-5.

[63] A. Kuş, Implementation of 3D Optical Scanning Technology for Automotive Applications, Sensors. 9 (2009) 1967–1979. https://doi.org/10.3390/s90301967.

[64] S.H. Yoon, A surface displaced from a manifold, in: Lect. Notes Comput. Sci. (Including Subser. Lect. Notes Artif. Intell. Lect. Notes Bioinformatics), Springer Verlag, 2006: pp. 677–686. https://doi.org/10.1007/11802914_56.

[65] G. Kocsis, C.J. Payne, A. Wallace, D. McNally, Wear analysis of explanted conventional metal back polyethylene glenoid liners, Med. Eng. Phys. 59 (2018) 1–7. https://doi.org/10.1016/j.medengphy.2018.03.010.

[66] Booleans, (n.d.). https://learn.foundry.com/modo/content/help/pages/modeling/edit_geometry/boolean.html (accessed November 11, 2020).

[67] FlexScan3D User Manual - Welcome, (n.d.). http://www2.lmi3d.com/manuals/flexscan3d/flexscan3.3.3/Default.htm (accessed November 12, 2020).

[68] MeshLab, (n.d.). https://www.meshlab.net/ (accessed November 13, 2020).

[69] CloudCompare, n.d.

[70] S. Gilbert, T. Chen, I.D. Hutchinson, D. Choi, C. Voigt, R.F. Warren, S.A. Maher, Dynamic contact mechanics on the tibial plateau of the human knee during activities of daily living, J. Biomech. 47 (2014) 2006–2012. https://doi.org/10.1016/j.jbiomech.2013.11.003.

[71] A. Liu, L.M. Jennings, E. Ingham, J. Fisher, Tribology studies of the natural knee using an animal model in a new whole joint natural knee simulator, J. Biomech. 48 (2015) 3004–3011. https://doi.org/10.1016/j.jbiomech.2015.07.043.

[72] N. Sancisi, M. Conconi, M. Forlani, V. Parenti-Castelli, A Test Rig for the Analysis of the Knee Under Dynamic Motion Tasks, J. Med. Device. 9 (2015) 020934. https://doi.org/10.1115/1.4030144.

[73] L.G. Sutton, F.W. Werner, H. Haider, T. Hamblin, J.J. Clabeaux, In vitro response of the natural cadaver knee to the loading profiles specified in a standard for knee implant wear testing, J. Biomech. 43 (2010) 2203–2207. https://doi.org/10.1016/j.jbiomech.2010.03.042.

[74] C.K. Fitzpatrick, P.J. Rullkoetter, Estimating total knee replacement joint load ratios from kinematics, J. Biomech. 47 (2014) 3003–3011. https://doi.org/10.1016/j.jbiomech.2014.07.002.

[75] P. Bowland, E. Ingham, J. Fisher, L.M. Jennings, Development of a preclinical natural porcine knee simulation model for the tribological assessment of osteochondral grafts in vitro, J. Biomech. 77 (2018) 91–98. https://doi.org/10.1016/j.jbiomech.2018.06.014.

[76] L. McCann, E. Ingham, Z. Jin, J. Fisher, An investigation of the effect of conformity of knee hemiarthroplasty designs on contact stress, friction and degeneration of articular cartilage: A tribological study, J. Biomech. 42 (2009) 1326–1331. https://doi.org/10.1016/j.jbiomech.2009.03.028.

[77] S. Affatato, M.C. Valigi, S. Logozzo, Wear distribution detection of knee joint prostheses by means of 3D optical scanners, Materials (Basel). 10 (2017). https://doi.org/10.3390/ma10040364.

[78] Y. Okazaki, M. Hosoba, S. Miura, T. Mochizuki, Effects of knee simulator control method and radiation dose on UHMWPE wear rate, and relationship between wear rate and clinical revision rate in National Joint Registry, J. Mech. Behav. Biomed. Mater. 90 (2019) 182–190. https://doi.org/10.1016/j.jmbbm.2018.09.034.

[79] A.E. Bowden, S.M. Kurtz, A.A. Edidin, Validation of a micro-CT technique for measuring volumetric wear in retrieved acetabular liners, J. Biomed. Mater. Res. Part B Appl. Biomater. 75B (2005) 205–209. https://doi.org/10.1002/jbm.b.30318.

[80] Polyga, HDI Advance 3D Scanner, n.d. www.polyga.com (accessed July 30, 2020).

[81] D. Shriram, E. Chosa, Y. Han, D. Lee, K. Subburaj, Effects of a valgus unloader brace in the medial meniscectomized knee joint: a biomechanical study, (n.d.). https://doi.org/10.1186/s13018-019-1085-1.

[82] T.J. Lujan, M.S. Dalton, B.M. Thompson, B.J. Ellis, J.A. Weiss, Effect of ACL Deficiency on MCL Strains and Joint Kinematics, (2007). https://doi.org/10.1115/1.2720915.

[83] ISO 14243-3, International Standard 14243-3: Implants for surgery - Wear of total knee-joint prostheses - Part 3: Loading and displacement parameters for wear-testing machines with displacement control and corresponding environmental conditions, 61010-1 © Iec2001. 2006 (2006) 13.

[84] International Standardization Organization, Implants for Surgery – Wear of Total Knee-joint Prostheses – Part 1: Loading and Displacement Parameters for Wear-testing Machines with Load Control and Corresponding Environmental Conditions for Test (14243-1), (2009).

[85] Density of Snowpeas (pea pod), raw in 285 units and reference, (n.d.). https://www.aqua-calc.com/page/density-table/substance/snowpeas-blank--op-pea-blank-pod-cp--coma-and-blank-raw (accessed November 3, 2020).

[86] S. Affatato, W. Leardini, M. Rocchi, A. Toni, M. Viceconti, Investigation on wear of knee prostheses under fixed kinematic conditions, Artif. Organs. 32 (2008) 13–18. https://doi.org/10.1111/j.1525-1594.2007.00455.x.

[87] M.E. Bowers, G.A. Tung, B.C. Fleming, J.J. Crisco, J. Rey, Quantification of meniscal volume by segmentation of 3 T magnetic resonance images, J. Biomech. 40 (2007) 2811–2815. https://doi.org/10.1016/j.jbiomech.2007.01.016.

[88] A. Thambyah, A. Nather, J. Goh, Mechanical properties of articular cartilage covered by the meniscus, Osteoarthr. Cartil. (2006). https://doi.org/10.1016/j.joca.2006.01.015.

[89] H.M.J. McEwen, J. Fisher, A.A.J. Goldsmith, D.D. Auger, C. Hardaker, M.H. Stone, Wear of fixed bearing and rotating platform mobile bearing knees subjected to high levels of internal and external tibial rotation, in: J. Mater. Sci. Mater. Med., Springer, 2001: pp. 1049–1052. https://doi.org/10.1023/A:1012850224565.

[90] K. Desloovere, P. Wong, L. Swings, B. Callewaert, H. Vandenneucker, A. Leardini, Range of motion and repeatability of knee kinematics for 11 clinically relevant motor tasks, Gait Posture. 32 (2010) 597–602. https://doi.org/10.1016/j.gaitpost.2010.08.010.

[91] V. Kefala, A.J. Cyr, M.D. Harris, D. Hume, Multiscale Modeling of the Human Musculoskeletal System View project, (2017). https://doi.org/10.1249/MSS.0000000000001350.

[92] C.K. Fitzpatrick, C. Maag, C.W. Clary, A. Metcalfe, J. Langhorn, P.J. Rullkoetter, Validation of a new computational 6-DOF knee simulator during dynamic activities, J. Biomech. 49 (2016) 3177–3184. https://doi.org/10.1016/j.jbiomech.2016.07.040.

[93] A. Szojka, K. Lalh, S.H.J. Andrews, N.M. Jomha, M. Osswald, A.B. Adesida, Biomimetic 3D printed scaffolds for meniscus tissue engineering, Bioprinting. 8 (2017) 1–7. https://doi.org/10.1016/j.bprint.2017.08.001.

APPENDIX A

Software Settings

Table 3. FlexScan3D scanning mode settings

Meshing				Rotatory		Easy Scan	
Generate	Alignment	Clean-Up	Mesh Density	# Scans	Auto Combine	HDR	High Sensitivity
Mesh	Mesh Geometry	Standard	20	8	Yes	Yes	No

Table 4. FlexScan3D combining and finalizing settings

Combine	Finalize		
Alignment	Merge	Sample Density	Hole Fill
Fine	Smooth	90	5

Table 5. MeshLab settings to clean and repair the meshed object

Compute Normals for Point sets		Surface reconstruction: Screened Poisson								
Neighbor num	Smooth Iteration	Recon Depth	Adaptive Octree Depth	Conjugate Gradients Depth	Scale Factor	Min Num of Samples	Interpolation Weight	Gauss-Seidel Relaxations	Confidence Flag	Pre-Clean
10	0	8	5	0	1.0	1.5	4	8	No	Yes

Table 6. CloudCompare setting for object alignment and Boolean difference (CGS)

Fine Registration Alignment (ICP)									Boolean Difference	
Aligned	Reference	RMS Difference	Final Overlap	Adjust Scale	Random Sampling Limit	Rotation	Translation	Enable Farthest Points removal	A	B
Tibia-Only	Tibia-Meniscus	1e-05	100	Yes	500,000	XYZ	Tx, Ty, Tz	Yes	Tibia-Meniscus	Tibia-Only

APPENDIX B

Digitized Data

Table 7. Digitized data analyzed before 250,000 cycles

	Before 250K Cycles						
	Initial Reference	Pre-Loading (Adjustment 1)	Difference	Initial Error (%)	Pre-Loading (Adjustment 2)	Difference	Final Error (%)
F-E	9.4	10.5	1.1	11.7	9.3	0.1	1.1
V-V	5.1	6.8	1.7	33.3	6.9	1.8	35.3
I-E	7.4	-0.8	8.2	111	8.0	0.6	8.1
M-L	0.5	0.3	0.2	40.0	0.5	0.0	0.0
A-P	-0.5	-0.7	0.2	40.0	-0.5	0.0	0.0
Axial	-1.9	-2.0	0.1	5.3	-1.9	0.0	0.0

Table 8. Digitized data analyzed after 250,000 cycles

	After 250K Cycles						
	Initial Reference	Post-Loading (Adjustment 1)	Difference	Initial Error (%)	Post-Loading (Adjustment 2)	Difference	Final Error (%)
F-E	9.4	10.2	0.8	8.5	9.3	0.1	1.06
V-V	5.1	5.7	0.6	11.8	5.9	0.8	15.7
I-E	7.4	3.1	4.3	58.1	8.0	0.6	8.1
M-L	0.5	0.5	0.0	0.0	0.5	0.0	0.0
A-P	-0.5	-0.5	0.0	0.0	-0.5	0.0	0.0
Axial	1.9	-1.9	0.0	0.	-1.9	0.0	0.0

Table 9. Digitized data analyzed after 500,000 cycles. Data was not recorded for pre-loading.

	After 500K Cycles			
	Initial Reference	Post-Loading	Difference	Error (%)
F-E	9.4	9.6	0.2	2.1
V-V	5.1	3.3	1.8	35.3
I-E	7.3	4.7	2.7	36.5
M-L	0.5	0.6	0.1	20.0
A-P	-0.5	-0.4	0.1	20.0
Axial	-1.9	-1.6	0.3	15.8

Table 10. Digitized data analyzed before 750,000 cycles

	Before 750K Cycles			
	Initial Reference	Pre-Loading (Adjustment 1)	Difference	Error (%)
F-E	9.4	4.5	4.9	52.1
V-V	5.1	4.0	1.1	21.6
I-E	7.4	5.4	2.0	27.0
M-L	0.5	0.6	0.1	20.0
A-P	-0.5	-0.5	0.0	0.0
Axial	-1.9	-1.8	0.1	5.3

Table 11. Digitized data analyzed after 750,000 cycles

	After 750K Cycles			
	Initial Reference	Post-Loading (Adjustment 1)	Difference	Error (%)
F-E	9.4	9.1	0.3	3.2
V-V	5.1	3.7	1.4	27.5
I-E	7.4	5.2	2.2	29.7
M-L	0.5	0.6	0.1	20.0
A-P	-0.5	-0.4	0.1	20.0
Axial	1.9	-1.8	0.1	5.3

Table 12. Digitized data analyzed before 1,000,000 cycles

	Before 1000K Cycles						
	Initial Reference	Pre-Loading (Adjustment 1)	Difference	Initial Error (%)	Pre-Loading (Adjustment 2)	Difference	Error (%)
F-E	9.4	8.9	0.5	5.3	8.6	0.8	8.5
V-V	5.1	3.9	1.2	23.5	4.0	1.1	21.6
I-E	7.4	5.2	2.2	29.7	5.1	2.3	31.1
M-L	0.5	0.6	0.1	20.0	0.6	0.1	20
A-P	-0.5	-0.5	0.0	0.0	-0.5	0.0	0
Axial	-1.9	-1.8	0.1	5.3	-1.8	0.1	5.3

Table 13. Additional data analyzed before 1,000,000 cycles

	Before 1000K Cycles						
	Initial Reference	Pre-Loading (Adjustment 3)	Difference	Initial Error (%)	Pre-Loading (Adjustment 4)	Difference	Error (%)
F-E	9.4	8.4	1.0	10.6	9.1	0.3	3.2
V-V	5.1	3.5	1.6	31.4	4.0	1.1	21.6
I-E	7.4	7.2	0.2	2.7	5.2	2.2	29.7
M-L	0.5	0.6	0.1	20.0	0.6	0.1	20.0
A-P	-0.5	-0.5	0.0	0.0	-0.5	0.0	0.0
Axial	-1.9	-1.8	0.1	5.3	-1.8	0.1	5.3

Table 14. Digitized data analyzed after 1,000,000 cycles

	After 1000K Cycles						
	Initial Reference	Post-Loading (Adjustment 1)	Difference	Initial Error (%)	Post-Loading (Adjustment 2)	Difference	Error (%)
F-E	9.4	8.8	0.6	6.4	8.8	0.6	6.4
V-V	5.1	3.1	2.0	39.2	3.2	1.9	37.3
I-E	7.4	5.7	1.7	23.0	5.6	1.8	24.3
M-L	0.5	0.7	0.2	40.0	0.7	0.2	40.0
A-P	-0.5	-0.4	0.1	20.0	-0.4	0.1	20.0
Axial	-1.9	-1.8	0.1	5.3	-1.8	0.1	5.3

Table 15. Additional digitized data analyzed after 1,000,000 cycles

	After 1000K Cycles			
	Initial Reference	Post-Loading (Adjustment 3)	Difference	Initial Error (%)
F-E	9.4	8.8	0.6	6.4
V-V	5.1	3.4	1.7	33.3
I-E	7.4	5.4	0.2	27.0
M-L	0.5	0.7	0.2	40.0
A-P	-0.5	-0.4	0.1	20.0
Axial	-1.9	-1.8	0.1	5.3